Grant Agreement No: 101096307

Full Title: THz Industrial Mesh Networks in Smart Sensing and Propagation Environments

Start date: 01/01/2023

End date: 31/12/2025

Duration: 36 Months

Deliverable D5.4

Development and validation of IRS-based THz links

Document Type	Deliverable
Title	D5.4
Contractual due date	30 June 2025 (M30)
Actual submission date	14 July 2025 (M30)
Nature	Report
Dissemination Level	PUB
Lead Beneficiary	CNRS
Responsible Author	G. Ducournau (CNRS)
Contributions from	Frédéric Dutin (CNRS), V. Torres (ANTERAL)

Revision history

Version	Issue Date	Changes	Contributor(s)
V0.1	13/06/2025	Initial version	G. Ducournau, F. Dutin (CNRS), V. Torres (ANT)
V0.2	29/06/2025	Sections revised and adds for R-IRS	V. Torres (ANT)
V1	06/07/2025	Characterization results of the R-IRS added	G. Ducournau, F. Dutin (CNRS)
V1.1	14/07/2025	Fixed items after Review by F. Meoni (BIREX)	F. Meoni (BIREX), G. Ducournau (CNRS)
V2	15/07/2025	Final review and acceptance	Luca Sanguinetti (CNIT), Thomas Kurner (TUBS)

Table of Contents

1. Introduction 7
1.1 Scope 7
1.2 Audience 7
1.3 Structure 7
2 Design and fabrication of IRS 8
2.1 IRS first prototype description 8
• Design procedure 8
• Fabrication and preliminary testing 10
2.2 IRS second prototype description 12
• Design procedure 12
• Fabrication and preliminary testing 13
2.3 Panel 15
2.4 Reconfigurable IRS 17
• State-of-the-art and LC physics 17
• LC synthesis 19
• Design 20
• Fabrication 22
• Raspberry Pi 24
• Voltage Generation Board 24
• IRS Support PCB 24
3 IRS Characterization 25
3.1 Method 25
• RS theory 25
• Description of the Experimental Setup 26
3.2 Results for RS first prototype 28
• RS Bandwidth Analysis using Specular Response Analysis 28
• Frequency band of the RS in the Nonspecular case 29
• Determination of the RS losses 30
3.3 Results for RS second prototype 31
• Experimental setup description 31
• RS bandwidth analysis by specular reflection analysis 31
• RS bandwidth analysis by nonspecular reflection analysis 32
• RS losses determination 33

3.4 Reconfigurable IRS 34
- Substrate response taken as reference 35
- Specular configuration 35
- Nonspecular configuration 36
- Conclusion of the R-IRS measurements 39

4 Terahertz Data-Links Including IRS 40
4.1 Testbed description 40
4.2 Fixed IRS 42
5 Conclusions 43
6 References 44

List of Abbreviations

THz	Terahertz
RS	Reflective Surface (Fixed-IRS, or static IRS)
IRS	Intelligent Reconfigurable Surface, or R-IRS
LoS	Line-of-Sight
NLoS	Non-Line-of-Sight
OTA	Over-the-Air
MEMS	Microelectromechanical Systems
VNA	Vector Network Analyzer
TRM	Thru, Reflect, Match
AoA	Angle of Arrival
AoD	Angle of Departure
B2B	Back-to-Back
MZM	Mach-Zehnder Modulator
QAM-16	Quadrature Amplitude Modulation 16 states
QPSK	Quadrature Phase Shift Keying
EDFA	Erbium Doped Fiber Amplifier
CW	Continuous Wave
UTC-PD	Uni-Traveling-Carrier Photodiode
SHM	Subharmonic Mixer
IF	Intermediate Frequency
EVM	Error Vector Magnitude

Executive Summary

This document offers a brief overview of the design, realization and characterization steps realized for intelligent reflective surfaces that were fabricated in the TIMES project. The achieved performances of the different prototypes are carefully determined and the impact of these related to the proof-of-concept demos targeted in the WP6.

1. Introduction

1.1 Scope

This deliverable provides a summary of the characterizations done for the different reflective surfaces designed and fabricated in the TIMES project.

In TIMES, 2 Proof-of-Concept (PoC) demonstrations are targeted, including over-the-air (OTA) propagation. In these PoCs, OTA in the 300 GHz band is supported by IRS, fixed or reconfigurable. These THz devices require specific characterizations and the THz transmission is also to be validated with the IRS. This last item is also part of this deliverable.

1.2 Audience

This Report is intended for primary use by the TIMES Consortium and public dissemination.

1.3 Structure

The rest of the document is structured as follows:

- Section 2 presents the IRS approaches considered and related designs.
- Section 3 proposes an overall description of the characterization steps and methods used for IRS performance assessment, applied for the 2 fixed prototypes and the reconfigurable one.
- Section 4 proposes the validation of the use of the reflective surface inserted in a THz link.
- Section 5 presents the main conclusions and impact of the IRS performances in the TIMES PoC1 and PoC2.

2 Design and fabrication of IRS

Within the scope of TIMES, developing a wireless network comparable to a wired one, especially in an industrial environment where the use of cooperative robots or real-time control is essential, requires addressing crucial concepts like data rate, accuracy, and reliability. To exceed the specifications of the 5G network, which are close but insufficient to meet these requirements, TIMES will exploit the capabilities of the THz spectrum for a 6G network. Among the challenges to ensure uninterrupted communications between various devices in an industrial setting, visual line-of-sight obstruction is one of the most intriguing to address. The use of IRS will not only solve this issue but also increase connectivity between machines without the need for additional antennas, resulting in overall lower power consumption and reduced maintenance costs. In the project, two different concepts of prototypes are managed: passive and active RS.

2.1 IRS first prototype description

- **Design procedure**

The purpose of the passive RS is to deflect an incoming beam toward a desired direction, bypassing obstacles that block the direct line-of-sight. The term "passive" indicates that no electronics are involved, and it does not steer the deflected beam in any direction other than the one for which it was designed.

The RS consists of an array of subwavelength elements (patches). By properly designing these patches, it is possible to change the reflected phase of an incoming beam to redirect it to a certain direction, rather than in the specular (geometric optics) direction. An array of elements where no phase difference between adjacent patches is observed would behave similarly to a metallic plane facing a plane wave with a non-normal incidence angle, i.e., following the standard law of reflection. For a linear phased array, a progressive phase difference between regularly spaced elements results in beam steering to a non-normal angle, due to the retardation of the wavefront on one side of the array with respect to the other.

As a first step, an analysis of the reflection phase and amplitude under broadside illumination and unit-cell boundary conditions is carried out for a series of square patches (width = w, height = h), as shown in Figure 1, to obtain a sufficiently large phase library. The phase excursion, at a certain frequency, will be the difference between the maximum and minimum achieved phase values

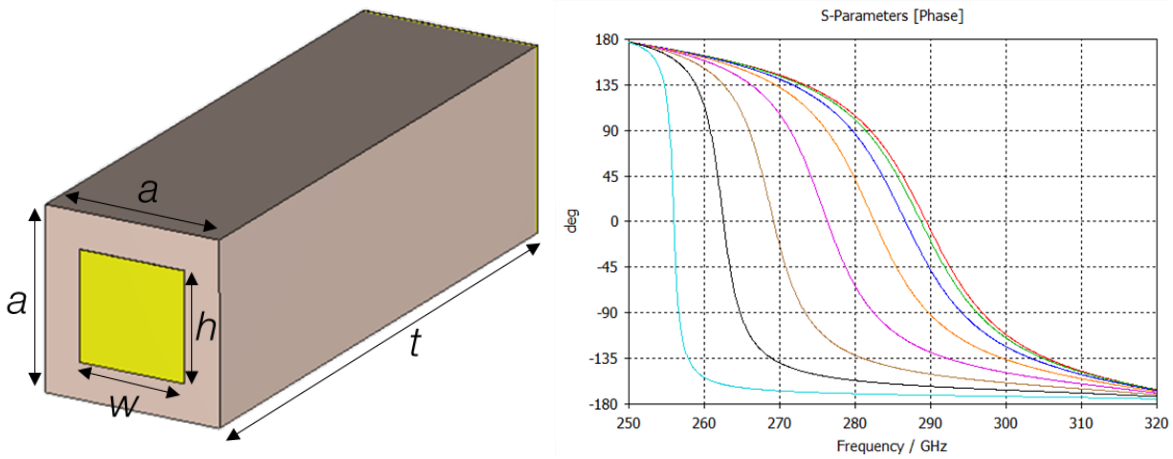

Figure 1 Unit Cell schematic, Design 1, and reflection phase for different patch dimensions (one color per patch response).

Initial broadband and patch/cell period dimension sweeps are necessary to obtain the patch dimension range for operation within the frequency range of interest for this development. Below, in Table 1, is a summary of the unit cell details. The material specifications for the substrate were obtained from Siegert Wafer.

Table 1 Specifications for the unit cell l, Design 1.

Substrate	
Material	Silicon
ε	11.9
Conductivity	0.01 [S/m]
Thickness, *t*	525 µm
Period, *a*	166.7 µm
Patches	
Material	Gold
Conductivity	4.561e+06 [S/m]
Dimensions, (*w* × *h*)	From 40×40 µm to 140×140 µm
Ground	
Material	Gold

After the unit cell simulation, an array simulation is performed. For a desired frequency (λ_0, wavelength), reflected angle θr and incident angle θi, two consecutive patches separated by a distance a (period) must have a phase difference of ΔØ (phase step):

$$\Delta Ø = 2\pi/\lambda_0 \ a\ (\sin\theta r - \sin\theta i\ )$$

Once the phase library is obtained for a certain period, the number of cells depends on the phase excursion and the phase step. Ideally, a 360º phase excursion must be swept from the first to the last patch of each subarray to have a smooth transition between them and avoid undesired lobes. The simulated RS array consists of 12×5 subarrays, each composed of 12 cells, as shown in Figure 2.

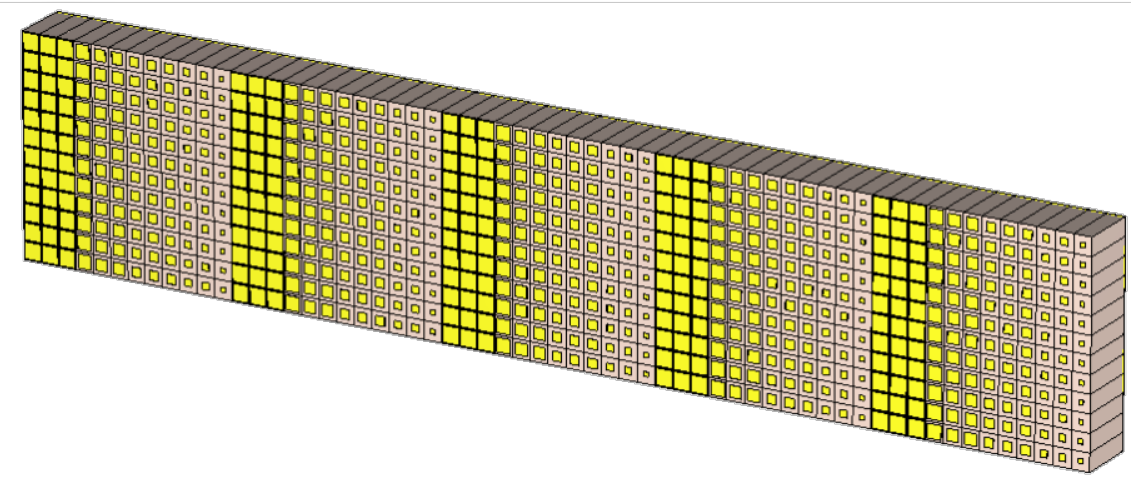

Figure 2 Schematic of the passive IRS, Design 1.

A broadside incidence, θi = 0º, and deflection to θr = −30º at f=275 GHz is considered. In Figure 3, the magnitude (in dB) of the φ = 0º far-field cuts (horizontal plane) from f = 275 GHz to f = 300 GHz (in 1 GHz

steps) is represented when the structure is illuminated with a plane wave. The best response is obtained at f = 281 GHz, slightly different from the design frequency. This frequency shift occurs because this simulation involves a finite structure, while the phase extraction from the patch simulations is done assuming infinite arrays. As observed, as the operating frequency is approached from both lower and higher frequencies, the specular (broadside for normal incidence) beam is reduced, and the θr = −30º beam appears. A beam at θr' = 30º is also found due to inaccuracies in the design process that are addressed with the second design. The low magnitude values of the scattered far fields are due to the fact that the simulated structure is actually very small, 10 mm × 2 mm. A larger structure was not simulated due to the computational resource requirements involved.

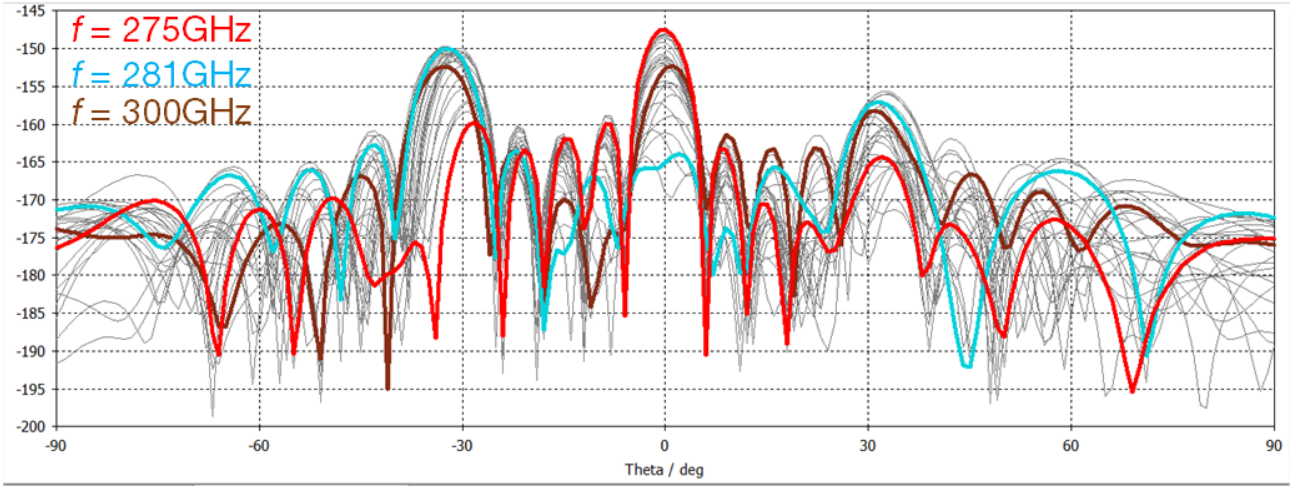

Figure 3 Radiation diagram cuts at φ = 0deg.

- **Fabrication and preliminary testing**

Once the design is finished, it is manufactured at the Public University of Navarre (UPNA) facilities. First, the pattern is etched onto photoresist by applying a layer of photoresist onto the 525 µm thick silicon wafer and exposing it to UV light.

Subsequently, the exposed photoresist is developed using a mild chemical developer and is ultimately removed with a stronger chemical stripper, leaving the circuit etched on it. The deposition of metals (20 nm Cr, 1 µm Cu and 30nm Au, same for patches and ground) is done by directly evaporating the metal in a chamber. This is achieved by reducing the chamber pressure to high vacuum, below 1e-5 torr, and then heating a crucible containing the metal until it evaporates. The cloud of evaporated metal vapor reaches the wafer and gently deposits onto it in a controlled way. It can take several hours to complete. Figure 4 shows the manufactured prototype with increasing detail.

Figure 4 Pictures of the manufactured RS.

To initially check the right working of the structure, some measurements are done. To measure the radiation characteIRStics of the prototype, the field (magnitude and phase) is recorded over a plane using a probe (OEWG, Open Ended Waveguide). The measurement plane must be large enough to avoid field truncation at the edges for proper conditions for the far-field transformation.

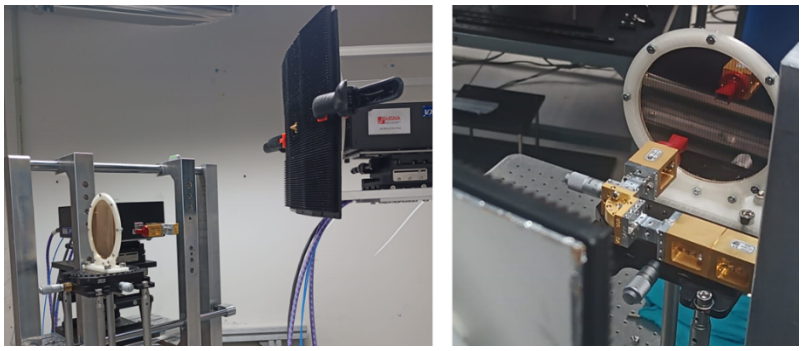

Figure 5 First measurement set-up at UPNA.

In Figure 6, the measured field amplitude is shown. The best response is obtained around 290 GHz. According to the experimental setup, under normal incidence, specular reflection is expected at X = 0 mm, while the beam is deflected around -200 mm. As observed in the figure, at f = 300 GHz, both specular and deflected beams coexist, whether at 290 GHz deflected beam is not even conformed. The fact that the better response, i.e, almost total reflection of the incident beam towards the desired angle (specular angle + 30º), is observed at f = 290 GHz, Figure 6, rather than at f = 275 GHz (theoretical calculation) or f = 281 GHz (numerical response), suggests that there are finite structure effects that must be considered in future designs.

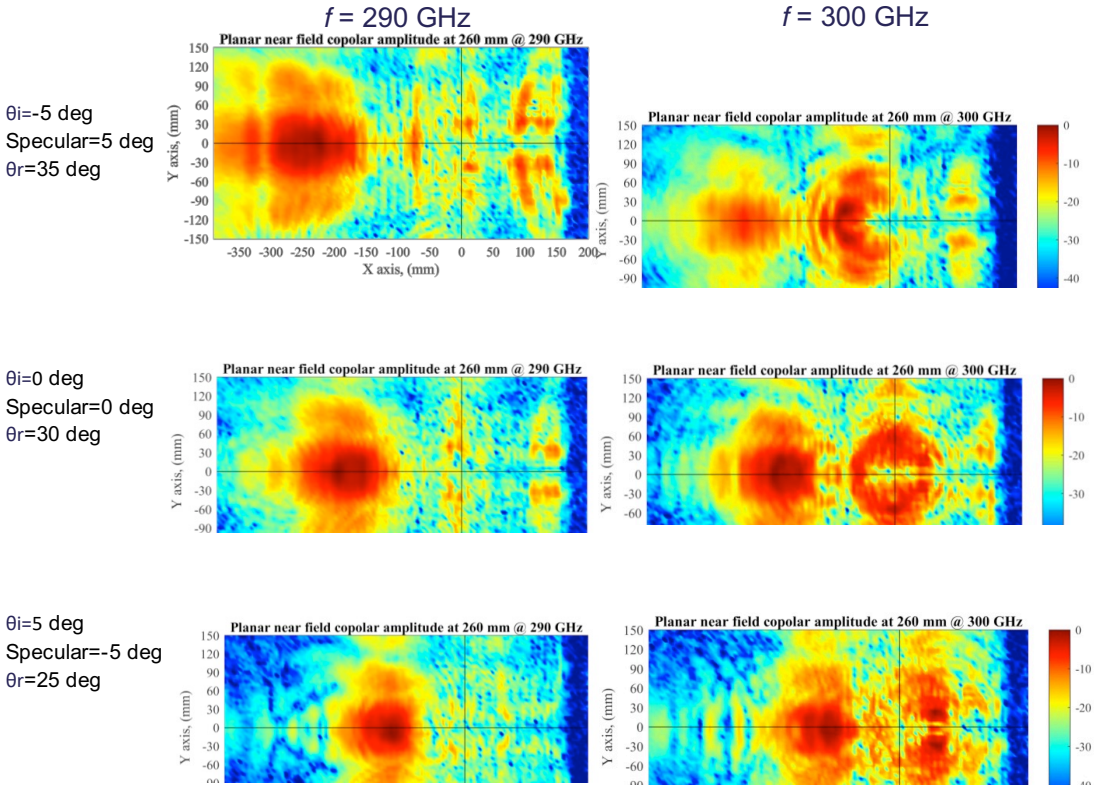

Figure 6 Near field values for different incident values @290GHz and @300GHz.

2.2 IRS second prototype description

- **Design procedure**

A new prototype is designed due to a review of the theoretical and numerical design process and the use of a different substrate material, more convenient from a purchase point of view (more stock and lower cost), as shown in Figure 7. First of all, as with the first prototype, the reflection phase and amplitude are analyzed under broadside illumination and unit-cell boundary conditions for a series of now rectangular (w × k) patches to obtain a large enough phase-library. Specifications of material and unit cell in Table 3.

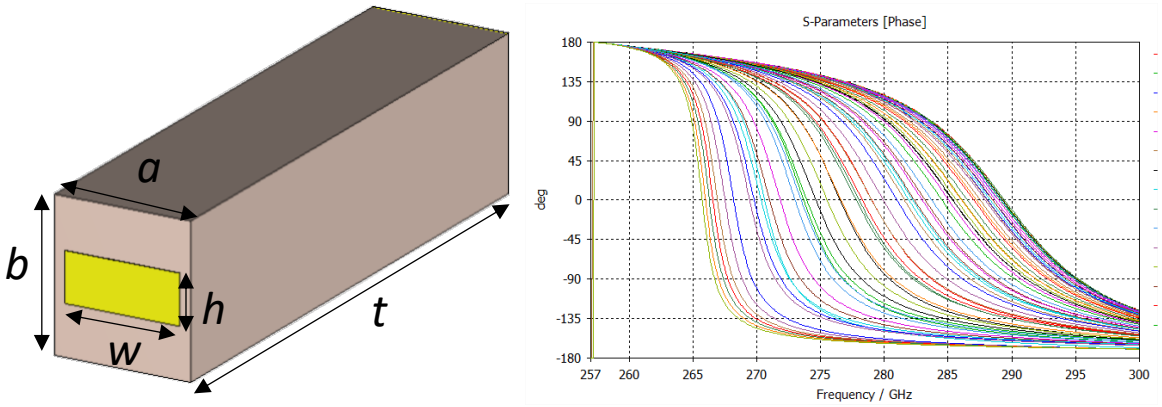

Figure 7 Unit Cell schematic, Design 2, and reflection phase for different patch dimensions.

Table 2 Specifications for the unit cell, Design 2.

Substrate	
Material	Silicon
ε	11.9
Conductivity	0.0002 [S/m]
Thickness, *t*	675 µm
Period, (*a* × *b*)	167 × 182 µm
Patches	
Material	Gold
Conductivity	4.561e+06 [S/m]
Dimensions, (*w* × *h*)	From 20×20 µm to 160×160 µm
Ground	
Material	Gold

The RS array simulated consists of 8 × 7 subarrays, each composed of 12 cells. A broadside (θi = 0º) incidence and deflection to θr = - 30º at f = 285GHz is considered for the unit cell calculation.

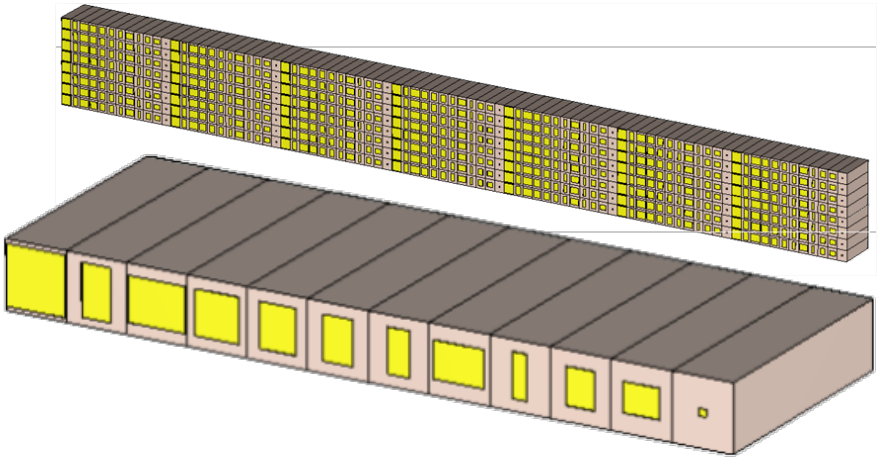

Figure 8 Schematic of the passive IRS, Design 2.

In Figure 9, the magnitude (dB) of three ϕ = 0º farfield cut planes (f = 260 GHz, f = 285 GHz and f = 300 GHz) are represented. As observed, as the operating frequency is approached from both lower and higher frequencies, the specular (broadside for normal incidence) lobe is reduced and the θr = -30º beam appears. The correction in the design process eliminated previously non desired beam at θr = 30º and the specular beam. The specular lobe is also of lower magnitude than in design 1.

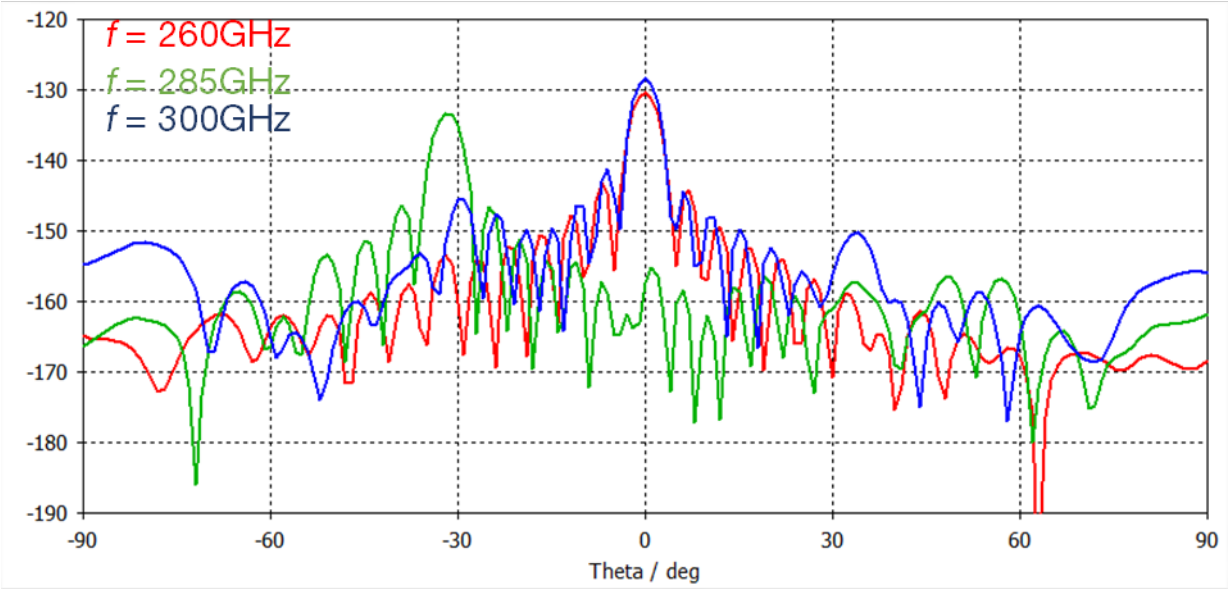

Figure 9 Radiation diagram cuts at φ = 0deg.

- **Fabrication and preliminary testing**

This second prototype is also manufactured at UPNA's facilities, following the same steps previously described. It is designed with a squared profile with its future incorporation into a 3x3 macro-array in mind that will be used in the PoC. Figure 11 shows the manufactured prototype, with the smallest patch (20 × 20 µm) shown in the inset.

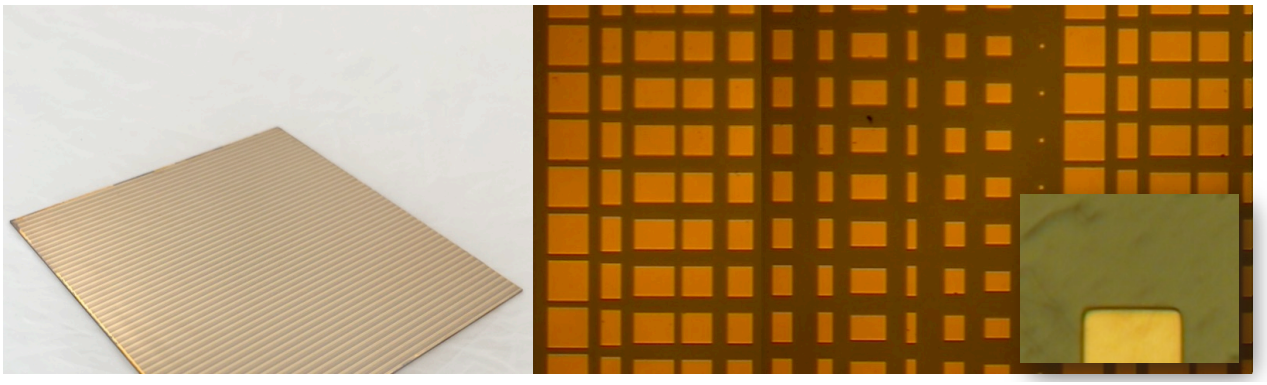

Figure 10 Manufactured prototype of the second design.

This second prototype is also initially characterized at the UPNA facilities in a similar way to the previous prototype. Figure 19 shows a photograph of the setup.

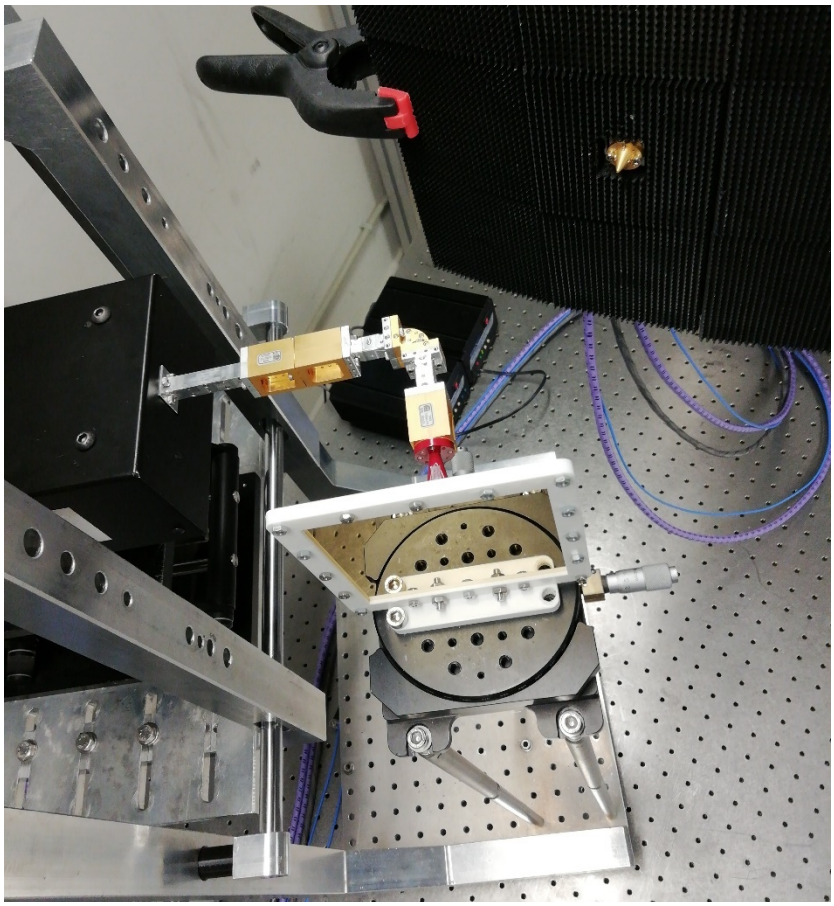

Figure 11 Second measurement setup at UPNA.

In Figure 12, the measured field can be observed with the near-field probe at 285 GHz under normal incidence. In this case, specular reflection is expected around 100 mm and the deflected angle at -50 mm. It is observed how most of the power is redirected towards the deflected angle, demonstrating that the structure works.

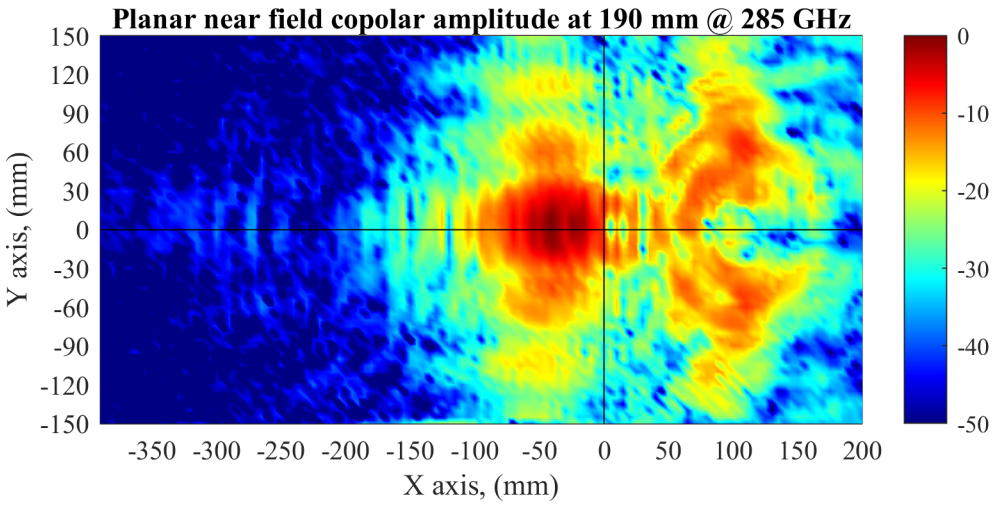

Figure 12 Planar near field copular amplitude of second prototype.

2.3 Panel

Previous prototypes have a limited size that may be insufficient for certain scenarios or communication links. Therefore, and with real proof-of-concept testing in mind, a panel has been created where several of these RS are grouped to form a larger RS. As described in the corresponding deliverable, one of the proofs of concept involves establishing communication through an IRS at 30 meters. At this distance, the high-gain antennas developed have a beamwidth of approximately 26 centimeters. Consequently, a 10 x 10 cm IRS is too small to redirect most of the transmitted power. This is why a larger panel has been created.

This panel consists of a 3 by 3 mosaic of the second prototype manufactured. The second prototype was chosen because, as will be seen in the next chapter, it has better absorption and loss performance. This panel, therefore, has a size of 30 x 30 cm, which allows it to capture most of the power emitted by the antenna.

The following figure shows the mechanical design of the structure supporting the panel.

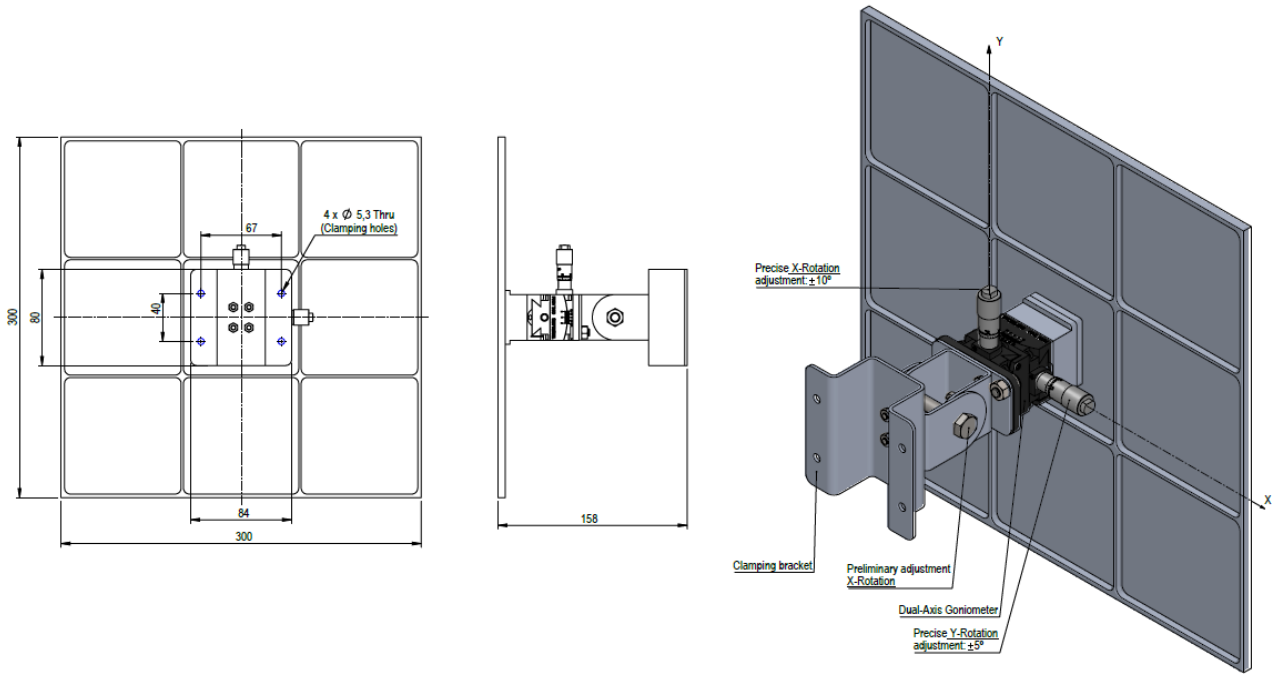

Figure 13 Mechanical drawing of the panel.

This structure features two goniometers for fine-tuning along both the vertical and horizontal axes. The panel can be tilted ±10º on the horizontal axis and ±5º on the vertical axis. This fine adjustment has a precision of one-tenth of a degree. This fine-tuning allows for adjusting the deflected angle to ensure correct antenna pointing. Additionally, there's a screw for coarser adjustment on the vertical axis, useful if the transmitting antenna, receiving antenna, and IRS are at significantly different heights.

The nine extra prototypes, fabricated from the second design, were attached to the panel using a two-component adhesive. During the prototype manufacturing, special attention was paid to the metallization of the wafer edges to minimize any edge effects. The following image displays several photographs of the complete panel with the RS (reconfigurable surfaces) adhered.

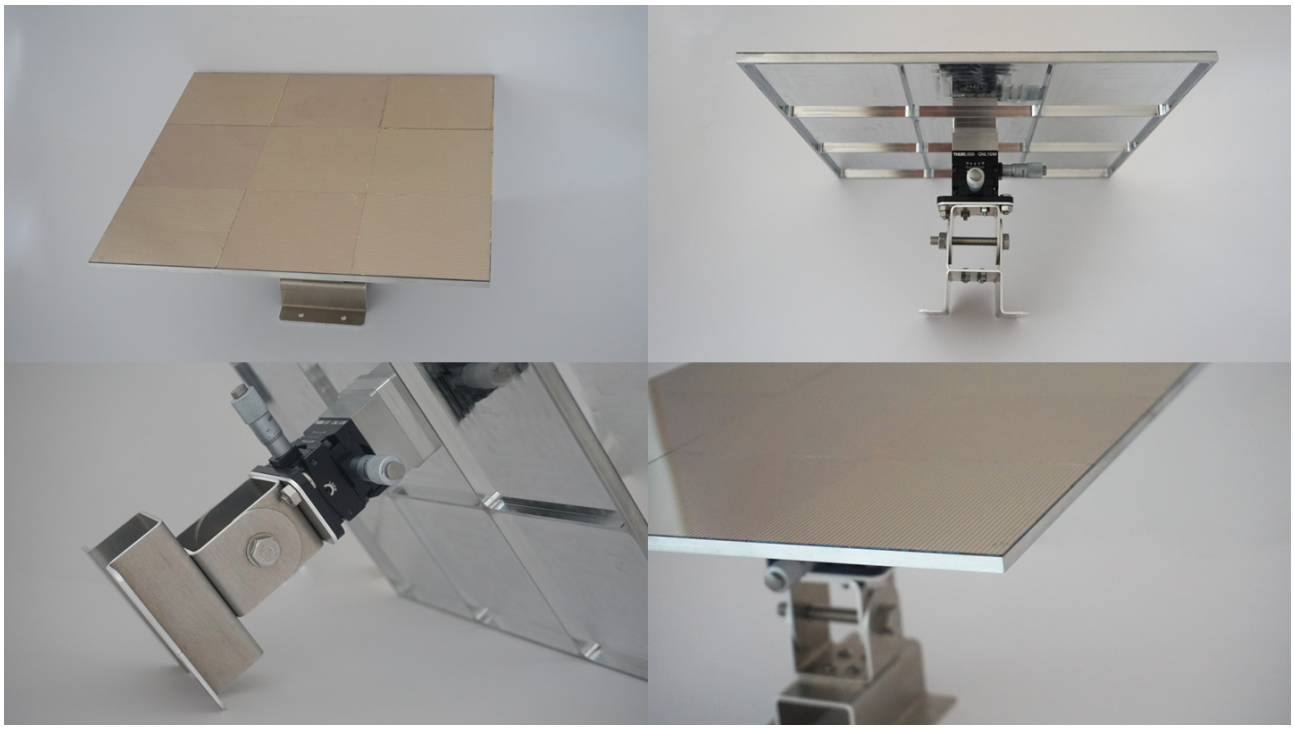

Figure 14 Photographs of the manufactured panel.

2.4 Reconfigurable IRS

- **State-of-the-art and LC physics**

The main difference between passive and active (or reconfigurable) IRS designs, technology-wise aside, is the ability to manipulate the reflection, refraction, or absorption of electromagnetic waves, dynamically adjusting their properties to optimize signal transmission or reception.

There are various ways to dynamically control the properties of an IRS. Essentially, all these methods involve controlling the transmission, reflection, and absorption properties of the individual elements that form the complete array. At frequencies above 100 GHz, this becomes an especially complex challenge where the inclusion of discrete electronic elements like diodes is impractical, and where other more "original" methods must be integrated. Some of these mechanisms can be:

1. Modulation by temperature. A high temperature superconducting film in the form of a split-ring resonator presents the capability of temperature-depending modulation of its transmission and tuning of its frequency resonance [1].
2. Bias-voltage-reconfigurable reflectarray. All radiating elements are geometrically identical, and the graphene patches in the same row are connected in series to a particular bias electrode. The phase response of the radiating elements can be controlled by changing the value of the bias voltage due to the property of the graphene of continuously steering its complex conductivity by applying a dynamical chemical potential, i.e. electric field [2].
3. Phase control by light. Reconfigurable terahertz metamaterial in which constituent resonators can be switched from split-ring resonators to closed-ring resonators via optical excitation of silicon islands strategically placed in the split gap, modifying the conductance of the gap [3].

4. Reconfigurable millimeter-wave reflectarray based on liquid-crystal (LC). By employing low losses LC composition and independent control of the unit cells in one dimension, a 1-D beam steering can be achieved.

The structure develop in TIMES is based on LC. The LC is a unique state of matter that exhibits properties of both liquids and solids. It consists of elongated or rod-shaped molecules that present a distinct orientation, but free to move within a certain range, that can be reoriented, for example, by an electric field. These orientations, Fig. 15, are:

- Crystaline Phase: molecules are organized in a regular, repeating structure in three dimensions, both in terms of position and orientation, fixed in a rigid lattice and without free movement.
- Smectic Phase: Molecules organized in layers, but within each layer, they exhibit nematic-like ordering.
- Nematic Phase: Molecules have an average orientation aligned in the same direction (called the director), but do not have positional order, although they can move and rotate freely like in a liquid.
- Liquid Phase: molecules do not have regular positional or orientational order and they can move and rotate freely, adapting to the shape of the container.
- Cholesteric (chiral nematic) Phase: Molecules spiral in a helical pattern. The chiral term refers to the chirality-exhibit phase, meaning the molecules have a specific handedness, either left-handed or right-handed.

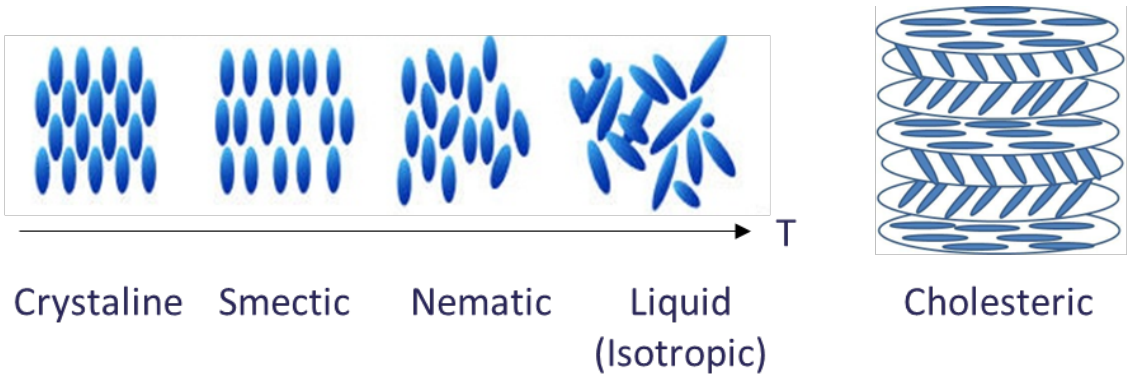

Figure 15 Different orientations of the molecule sin the Liquid Crystal.

This material is temperature sensitive, and heating may change a crystal into a liquid, whereas cooling may induce liquid crystalline phases. When a LC layer is first manufactured, the molecules undergo an initial alignment that can be done by one of many techniques available: rubbing, photoalignment, electric field alignment.

Different molecule orientation implies different ϵ, as the molecules interact differently with an incident electric field. Thus, by means of a certain voltage-frequency combination (that generates a polarizing electric field) it is possible to achieve different ε, modeled using a complex permittivity tensor:

$$\bar{\bar{\varepsilon}}\,(V_b = 0) = \begin{bmatrix} \varepsilon_\perp & 0 & 0 \\ 0 & \varepsilon_\parallel & 0 \\ 0 & 0 & \varepsilon_\perp \end{bmatrix}, \qquad \bar{\bar{\varepsilon}}\,(V_b = V_{max}) = \begin{bmatrix} \varepsilon_\perp & 0 & 0 \\ 0 & \varepsilon_\perp & 0 \\ 0 & 0 & \varepsilon_\parallel \end{bmatrix}.$$

Thus, for molecules initially (voltage = 0) oriented parallel to the surface, the application of a maximum voltage (defined by the LC manufacturer) would orient the molecules perpendicularly to the surface, exhibiting an overall different permittivity.

So, the underlying idea in the design of LC-based IRS is that, by placing the array of elements on a layer of LC (liquid crystal), the local permittivity that each simple element of the array experiences can be controlled by applying a bias voltage to the LC.

- **LC synthesis**

The most promising class of liquid crystalline compounds for creating nematic LC compositions with high birefringence are linear polycyclic liquid crystalline compounds, in particular derivatives of terphenyl and quaterphenyl with various terminal and lateral substituents, which can be represented by the following general structural formula:

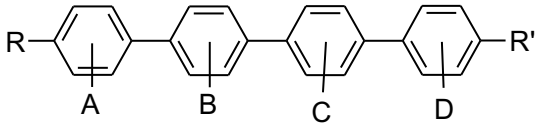

These compounds have rod-shaped molecules and are characterized by good miscibility with all known low-viscosity classes of LC compounds. These compounds are characterized by fairly high optical anisotropy values and can find application in corresponding liquid crystal mixtures. Derivatives of this type (ter- and quaterphenyls) are obtained, as a rule, according to classical schemes involving the interaction of Grignard reagents based on biphenyl derivatives with the corresponding 4-iodo-substituted biphenyls in the presence of complex nickel catalysts.

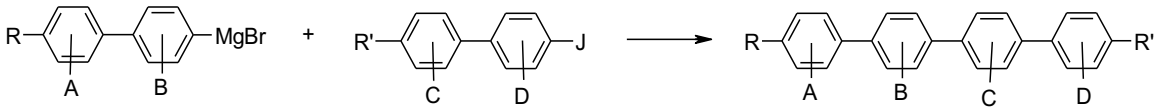

Instead of Grignard reagents, the more reactive organolithium biphenyl derivatives obtained by treating the corresponding aryl halides with butyllithium can also be used.

Recently, for the synthesis of aromatic polycyclic derivatives of ter- and quaterphenyl, methods involving catalytic cross-coupling of individual fragments of the molecule (Suzuki reaction) have been mainly. Palladium complexes are typically used as catalysts for cross-coupling. Various variations of cross-coupling are known, such as:

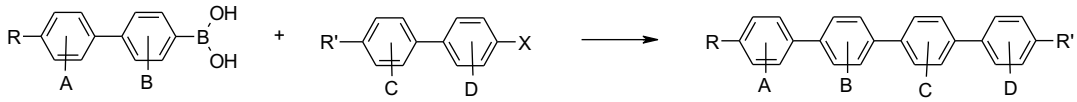

where X = Br, J, OSO_2CF_3; A, B, C, D = lateral substituents.

Using these traditional approaches, a fairly wide range of polycyclic aromatic LC compounds, which are derivatives of ter- and quaterphenyl, have been synthesized.

A new approach to the synthesis of relatively low-melting laterally substituted tetracyclic LC compounds, quaterphenyl derivatives, based on the use of the Mannich salt condensation reaction with substituted methyl benzyl ketones as a key step have been developed. The synthetic scheme involves the use of relatively available 4-acetyl-4-alkylbiphenyls (1) as the starting compound.

In total, 9 new compounds as the best candidates for the preparation of high birefringence LCMs have been synthesized. With the 9 compounds synthesized, two LC mixtures are prepared. When developing the LC

compositions for our purpose, it was necessary to achieve the maximum possible value of optical anisotropy, since this parameter greatly affects the efficiency and maximum tunability. For further experiments, in order to broaden the temperature range of the nematic phase and increase the optical anisotropy, two LC compositions based on three- and four-ring LC compounds were prepared with an optical anisotropy value of about 0.34.

The measured properties of the LC mixtures are shown in the next table. For the final device, LCM-1 is used.

Table 3. *Physical properties of prepared LC mixtures*

Optical anisotropy (589 nm, 25°C)	LCM-1	0.349
	LCM-2	0.342
Dialectical anisotropy (1 kHz, 25°C)	LCM-1	10.8
	LCM-2	10.2
Threshold voltage (25°C)	LCM-1	1.95 V
	LCM-2	2.03 V
Saturation voltage (25°C)	LCM-1	3.2 V
	LCM-2	3.27 V
Melting point	LCM-1	- 6.3 °C
	LCM-2	- 7.4 °C
Clearing point	LCM-1	+ 98.5 °C
	LCM-2	+ 87.6 °C

- **Design**

Similarly to the passive case, first an analysis of the reflection phase and amplitude under broadside illumination and unit-cell boundary conditions was carried out.

The unit cell is shown in Figure 16. A line connects each cell in the subarray with the one above and below and feeds each column with a certain voltage given by an electrode. This bias voltage fixes the ε of the LC in the area below the patches of the same column (which affects the reflected phase). The permittivity is modeled with the complex permittivity tensor above shown and manually changed depending on the intended orientation of the molecules (from β=0º, parallel to the patch and LC surface, to β=90º). A quartz layer seals the LC and prevents it from leaking.

The phase excursion at a certain frequency will be the difference between the maximum and minimum achieved phase values, which will correspond with the maximum and minimum values for ε, provided by the LC manufacturer.

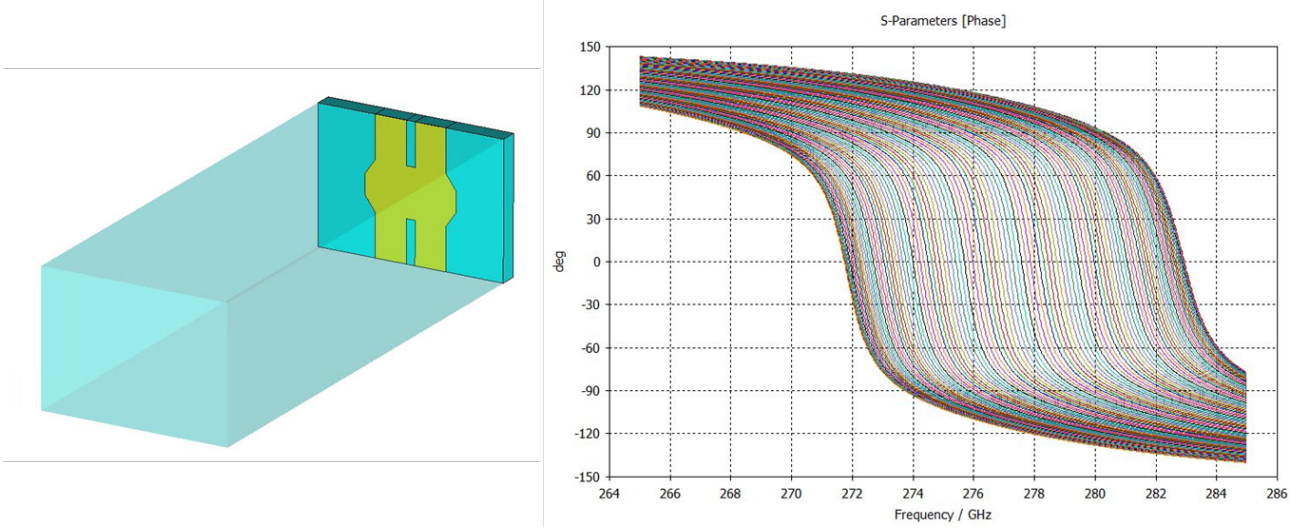

Figure 16. LC Unit Cell schematic and reflection phase for different bias voltages.

Table 4. *Specifications for the LC unit cell*

Substrate	
Material	Liquid Crystal
ε	From 2.685 to 3.715
Thickness	40 μm
Unit cell period	300 × 420 μm
Patches	
Material	Gold
Conductivity	4.561e+06 [S/m]
Ground	
Material	Gold
Quartz	
Thickness	1.08mm

The full IRS array consists of 214 electrodes or columns where all elements of the same electrode are connected. The electrodes are grouped with a periodicity of 5 elements. This means that only 5 different voltages are applied to the 214 electrodes. Therefore, the phase response is repeated in each subarray, that creates the full response of the IRS.

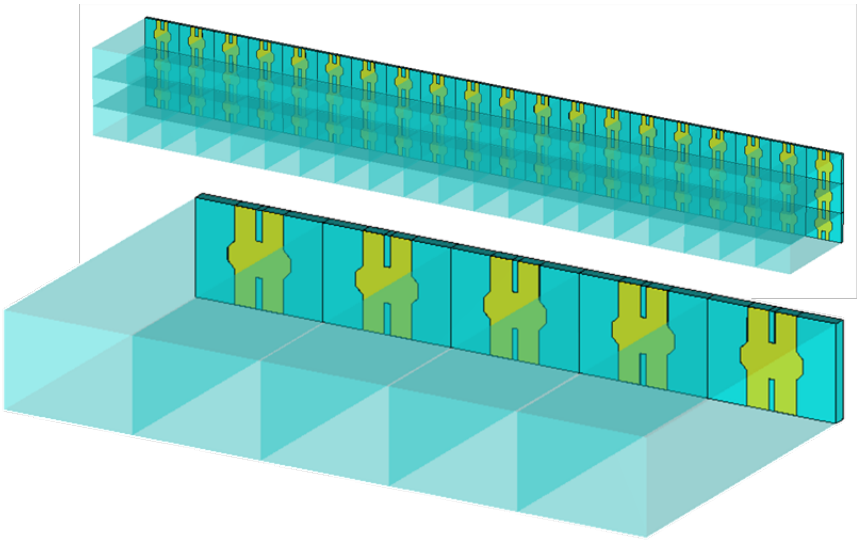

Figure 17. Portion of the LC IRS and detail of a subarray.

The voltage of each electrode and, therefore, the phase of each unit cell, is designed so that, under normal incidence, the subarray reflects with a deflected angle of 30 degrees. The following figure shows the far-field simulation results for the φ = 0º cut for different frequencies. It can be observed that as the operating frequency is approached, the specular reflection decreases, and only the peak corresponding to the deflected angle remains.

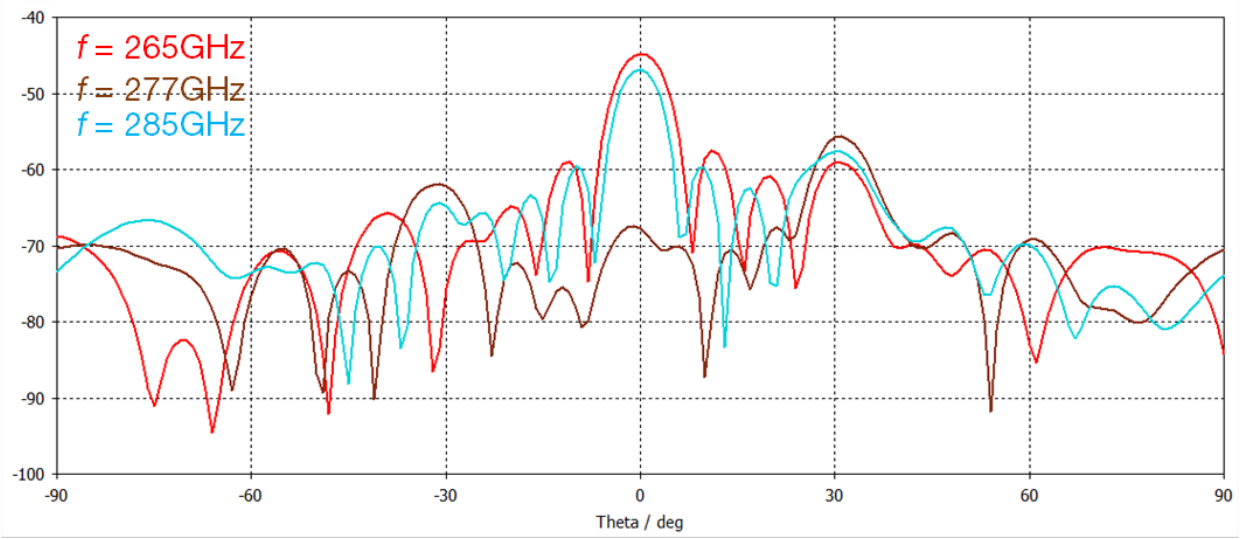

Figure 18. Radiation diagram cuts at φ = 0deg.

- **Fabrication**

To implement electro-optical effects in LC, it is necessary to manufacture a special cell. This cell is a flat capillary made in the form of two plane-parallel substrates, on the inner sides of which conductive and orienting layers are sequentially applied. The cell is filled with an LC with positive dielectric anisotropy.

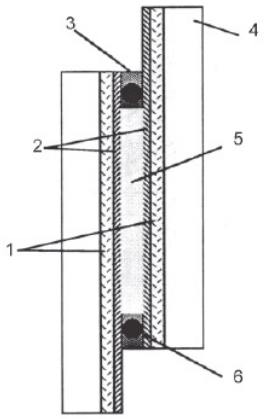

1 - conductive coating, 2 - orienting layer, 3 - sealant, 4 - substrate, 5 - LC layer, 6 - spacer

Figure 19. Basic design of an LCD cell

The liquid crystal matrix consists of two substrates with a conductive coating (of a certain pattern), separated by spacers, and a liquid crystal material placed between them. The substrates were cleaned with organic solvents to remove dust and other surface contaminants. A thin polymer layer was then applied to the surface of each substrate to orient the liquid crystal molecules. The application of the orienting layer was carried out by centrifugation (Figure 19).

After application and imidization (cyclization of the amido acid into polyimide), the orienting layer was rubbed with a soft fleecy cloth using a special machine to set the required planar orientation of the liquid crystal molecules. Spacers were used to ensure a uniform gap between the substrates. The treated substrates with applied spacers were placed together and glued around the perimeter. Next, the matrices were filled with liquid crystal material.

The deposition of the metallic array is carried out using photolithography, and the electrodes are connected to a PCB where the contacts and power supply lines, which terminate in standard connectors, have been milled. The entire structure is assembled within a plexiglass frame secured by various screws that ensure the elements are fixed. Figure 20 shows photographs of the assembled prototype.

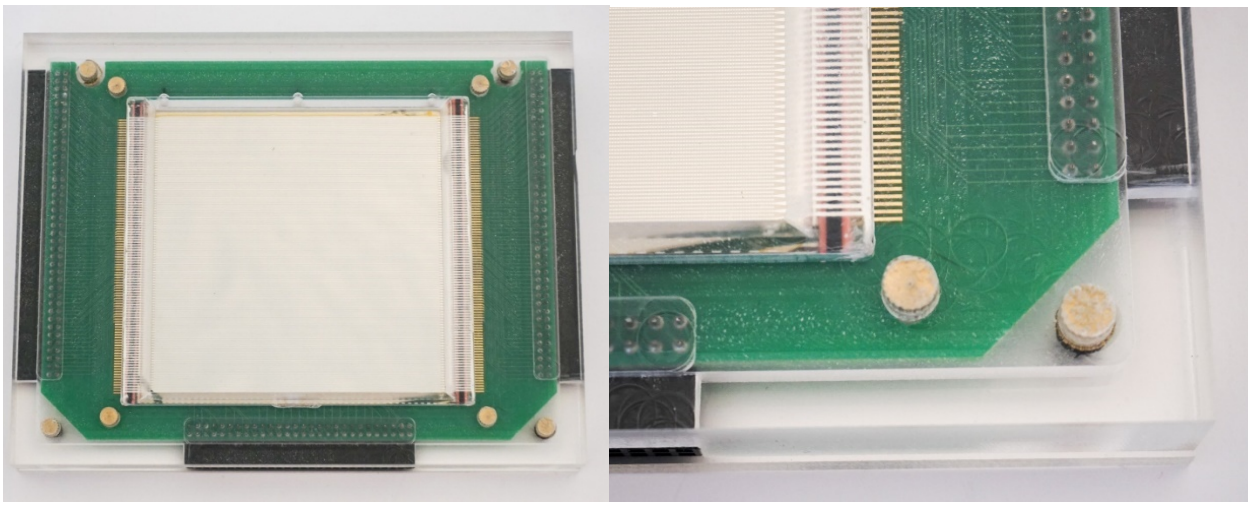

Figure 20. Reconfigurable IRS (R-IRS) prototype

The control electronics were also designed and manufactured independently. These electronics consist of three sub-elements:

- Raspberry Pi

A Raspberry Pi is responsible for generating a 1 kHz square wave signal with a voltage between 0-3.3V. This signal serves as the base for generating the five necessary voltages that power the IRS.

- Voltage Generation Board

With an input voltage of 12V DC, a second electronics board generates the five necessary voltages to power the IRS from the 1 kHz signal. These voltages are conditioned to vary between negative and positive values, with a maximum peak-to-peak voltage of 15V. A manual potentiometer allows for varying the amplitude of these voltages, thus achieving the desired voltage variation applied to the electrodes.

- IRS Support PCB

A third PCB supports the IRS and distributes the five supply voltages among the electrodes. This PCB includes a power distribution network designed to maintain the necessary periodicity in accordance with the electromagnetic simulation.

Figure 21 shows these three elements and IRS assembled on a plexiglass plate.

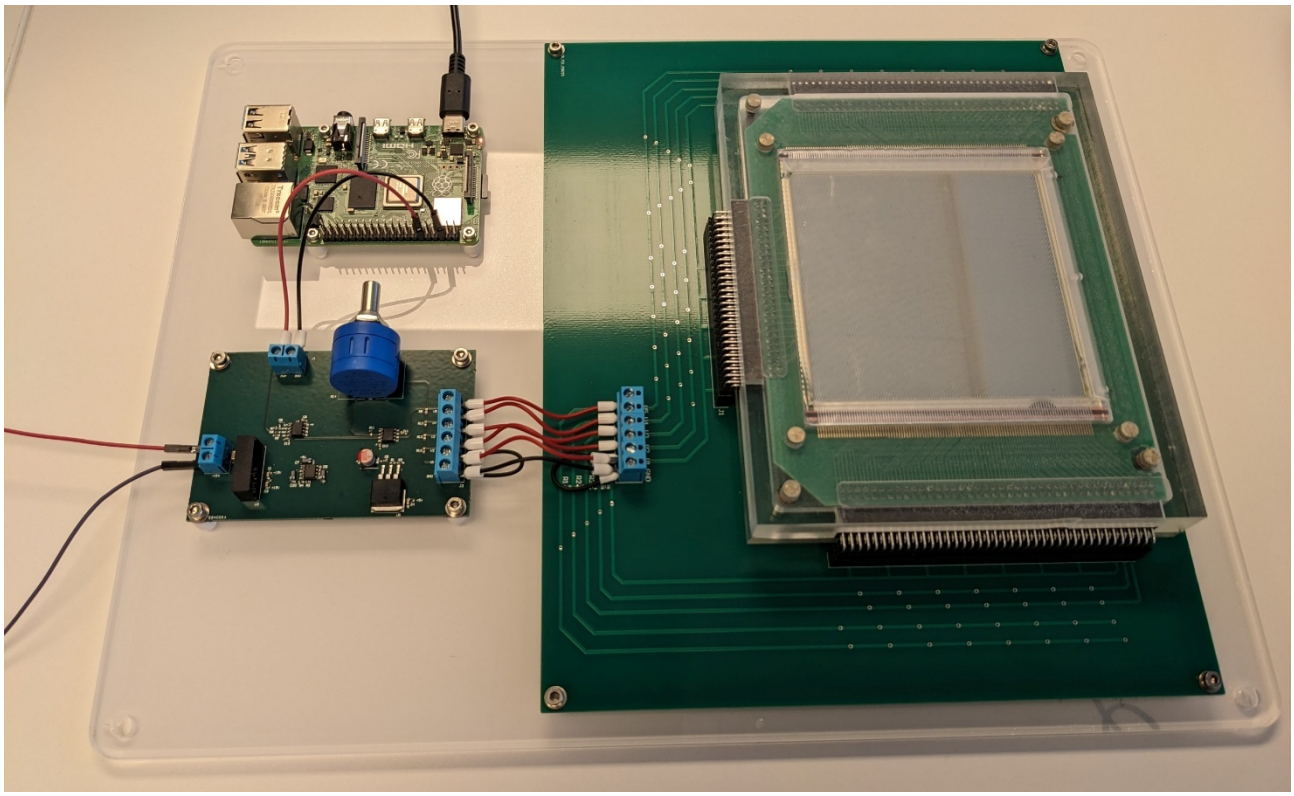

Figure 21. IRS and control electronics

3 IRS Characterization

In this section, we are presenting a work which has been published under the name “Non-line-of-sight 300 GHz band Wireless link enabled by a frequency dependent reflective surface” by Frédéric Dutin, Unai Beaskoetxea, Victor Torres, Pascal Szriftgiser, Jorge Teniente and Guillaume Ducournau in *IEEE Transactions on Terahertz Science and Technology* (2025).

3.1 Method

- **RS theory**

Prior to characterization, simulations using Floquet modes were done in order to find the maximum nonspecular reflection angles induced by the passive IRS or Reflective Surface (RS) related to a defined incident angle, operating frequency and the periodicity of the RS. If the RS is illuminated by a plane wave, the x-component of the mth Floquet harmonic is defined as the tangential wavenumber of the reflected plane wave harmonic, k_{xm}, along the x-axis as

$$k_{xm} = k_{x0} + \frac{2m\pi}{d_x}, \tag{1}$$

where $k_{xm} = k \sin\theta_{\mathrm{AOD},m}$ and $k_{x0} = k \sin\theta_{\mathrm{AOA}}$. k is the operating wavenumber, $\theta_{\mathrm{AOD},m}$ and θ_{AOA} are the angle of departure for the mth Floquet mode and the RS's illuminating plane wave angle of arrival with respect to the normal of the RS, respectively. The basic array size d_x determines the ability of the RS to reflect into multiple angles depending on θ_{AOA} and $\theta_{\mathrm{AOD},m}$. The maximum reflection angle for the mth Floquet harmonic $\theta_{\mathrm{AOD},m}$ is then determined by

$$\sin\theta_{\mathrm{AOD},m} = \sin\theta_{\mathrm{AOA}} + \frac{m\lambda}{d_x}, \tag{2}$$

where $\lambda = 2\pi/k$ is the operating wavelength. Because of (2), only a finite number of propagating plane wave modes significantly contribute to the field. The additional higher-order (evanescent) modes do not contribute as their propagation constants in the normal direction are imaginary. Controlling the propagating Floquet modes via the periodicity of the RS and the incident angle enables accurate prediction of reflection amplitudes, without the need for full-wave electromagnetic simulations.

The range of operating frequencies is between 220 and 325 GHz, as shown in the next section. Satisfying $|k_{xm}| < k$, there are four, five, or six propagating harmonics depending on the frequency with $m = 0, \pm1, \pm2, -3$. Specular reflections are given by the mode $m = 0$ whereas anomalous reflections are given for $m \neq 0$. Nevertheless, in our configuration, only reflection angles between 20° and 70° with respect to the normal of the RS are measured. Since they correspond to the Floquet mode $m = 1$, maximum reflection angles for each frequency of interest are thus calculated by the use of (2), with $m = 1$, as shown in Figure 22. For $\sin\theta_{\mathrm{AOA}}$ less or equal to 30°, we see that the more the frequency increases, the more the reflection angle decreases. In Figure 22, we focused on the frequency range between 270 and 320 GHz where maximum insertion losses values occur, as it will be seen later (cf. Figure 26).

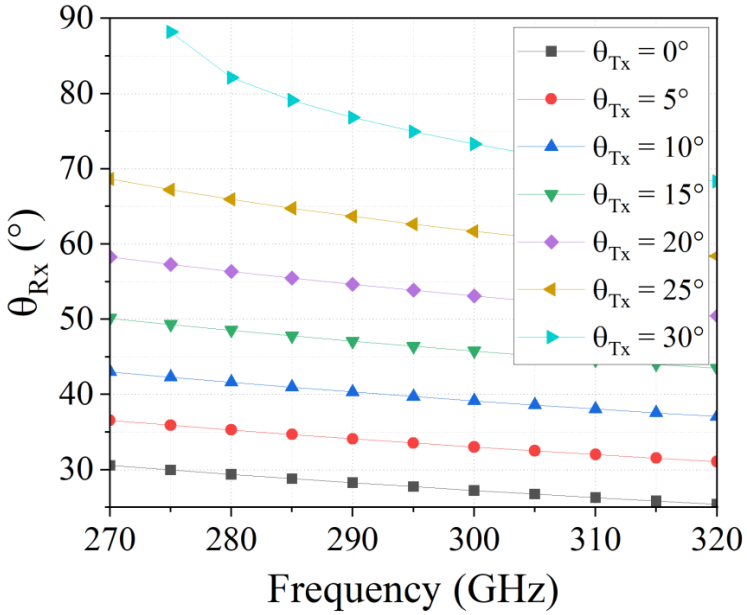

Figure 22. Maximum reflection angles given by the Floquet mode $m = 1$ theory.

- **Description of the Experimental Setup**

Figure 23(a) shows the RS during performance characterization measurements in free space with a 220-325 GHz VNA. The RS is fixed onto a first rotating platform. The incident port of the VNA is in a fixed position while the reflected port is placed on a breadboard coupled to a rotating platform. Both rotating platforms have a rotation range of $360°$. With this configuration, they can be adjusted independently and we used them manually during acquisitions. To achieve the required THz alignments, both rotation stages have the same rotation axis. In the following, both sides of the RS are used. the front side is the frequency-dependent RS, and the backside is composed of pure metal and will be used as reference.

First, the VNA is calibrated using waveguide standards, using the TRM (Thru, Reflect, Match) method [4]. Doing so, the calibration plane is then set at the WR3.4 VNA outputs (cf. Fig. Figure 23(a)). Then, over-the-air (OTA) measurements are enabled by connecting horn antennas at both VNA outputs. These standard horns are connected on each port of the VNA and are at the same height as the center of the RS. In order to illuminate the RS with known k-vector direction, the beams are collimated by using two THz lenses. These lenses (diameter 25 mm, focal length 25 mm) are placed in front of horn antennas. The distance between horn and lens is adjusted to get the lens focal point corresponding to the phase-center of each horn antenna. The collimated beam is then illuminating the RS, deflected and collected again by the second lens (L2). The distance between the lenses and the RS is about 125 mm.

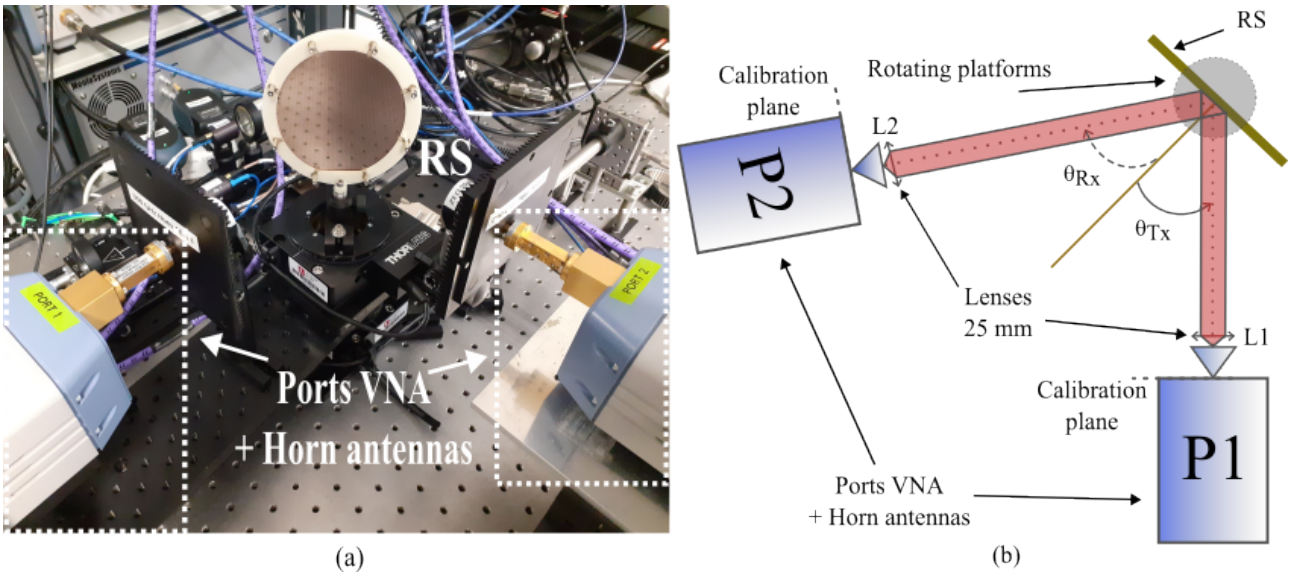

Figure 23. (a) Photo and (b) drawing of the VNA experimental setup.

The antenna gains over the WR3.4 band were checked prior to experiment. For this, the two identical horns are aligned and gain calculated from S_{21} and the usual Friis equation. The typical gain is shown in Figure 24.

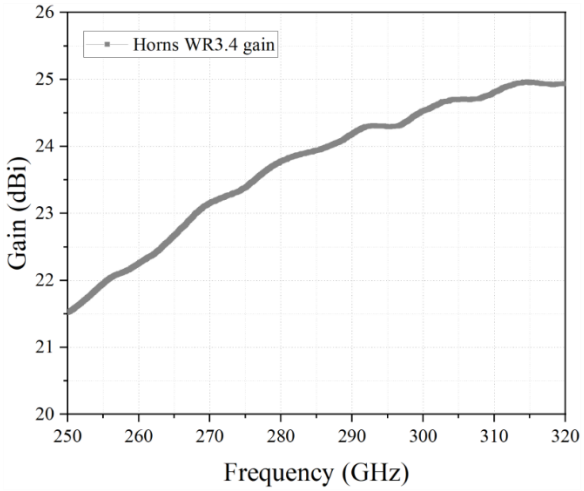

Figure 24. Horn antenna gain (Horn input is a WR3.4 waveguide).

In Figure 23(b), θ_{AOA} and θ_{AOD} are the angle of arrival and the angle of departure with respect to the normal of the RS, respectively. Angles are adjusted using rotation stages with a 5° step (identical for θ_{AOA} and θ_{AOD}) and are swept from 0° to 45° for θ_{AOA} and from 20° to 70° for θ_{AOD}. According to the testbed configuration, the specular reflection can be measured for $\theta_{\mathrm{AOA}} = \theta_{\mathrm{AOD}}$ from 20° to 45°, enabling to assess the impact of the incident angle on RS's absorption bandwidth discussed in the next section. Then we measured the S_{21} parameter for all different angles couples $(\theta_{\mathrm{AOA}}, \theta_{\mathrm{AOD}})$ which are noted in Table 5. Gray cells correspond to specular configurations, where $\theta_{\mathrm{AOA}} = \theta_{\mathrm{AOD}}$. As shown in Table 5, we did 36 measurements for both RS and metallic backside of the RS for reference. For each value of θ_{AOD}, we rotated the RS to change θ_{AOA} and acquired the S_{21} amplitude and phase.

Table 5. Couple of angles for insertion loss measurements. Gray cells correspond to specular configurations

$(\boldsymbol{\theta_{AOA}, \theta_{AOD}})$					
$\boldsymbol{(20, 20)}$	(25,25)	(30,30)	(35,35)	(40,40)	(45,45)
$\boldsymbol{(15, 25)}$	(20,30)	(25,35)	(30,40)	(35,45)	(40,50)
$\boldsymbol{(10, 30)}$	(15,35)	(20,40)	(25,45)	(30,50)	(35,55)
$\boldsymbol{(5, 35)}$	(10,40)	(15,45)	(20,50)	(25,55)	(30,60)
$\boldsymbol{(0, 40)}$	(5,45)	(10,50)	(15,55)	(20,60)	(25,65)
$\boldsymbol{(-5, 45)}$	(0,50)	(5,55)	(10,60)	(15,65)	(20,70)

3.2 Results for RS first prototype

- **RS Bandwidth Analysis using Specular Response Analysis**

First, we compared S_{21} amplitudes of specular reflections for the RS and for the metallic plate (RS back-side) for different incident angles. Before any interpretations, the curves we measured were particularly affected by standing wave due the quasi-optic configuration rather than induced by the RS. Thus, we smoothed all of them by using a Savitzky-Golay filter of degree 3 where the span is about 20 points for a 5 GHz spectral range to obtain Figure 25(a)-(f) and Figure 26(a)-(e).

In Figure 25(a)-(f), we note that in the specular case, the metal plate and the RS got almost the same S_{21}. Thus, the RS is not absorbing anything between 220-270 GHz and 315-325 GHz (mirror-like behavior). Nevertheless, from 270 GHz to 315 GHz, for each incident angle, we have a clear absorbing behavior with a decreased S_{21} up to a 15 dB absorption level. However, the incident angle seems to play a role related to the range of absorbed frequency (AF) range. In the proposed method, the determination of the RS absorbing frequency range in the specular case provides the basis of the next analysis which focus on the nonspecular behavior of the RS. Indeed, the RS nonspecular operation frequency bandwidth should correspond to the RS specular absorption band, which is to be determined prior to the nonspecular analysis.

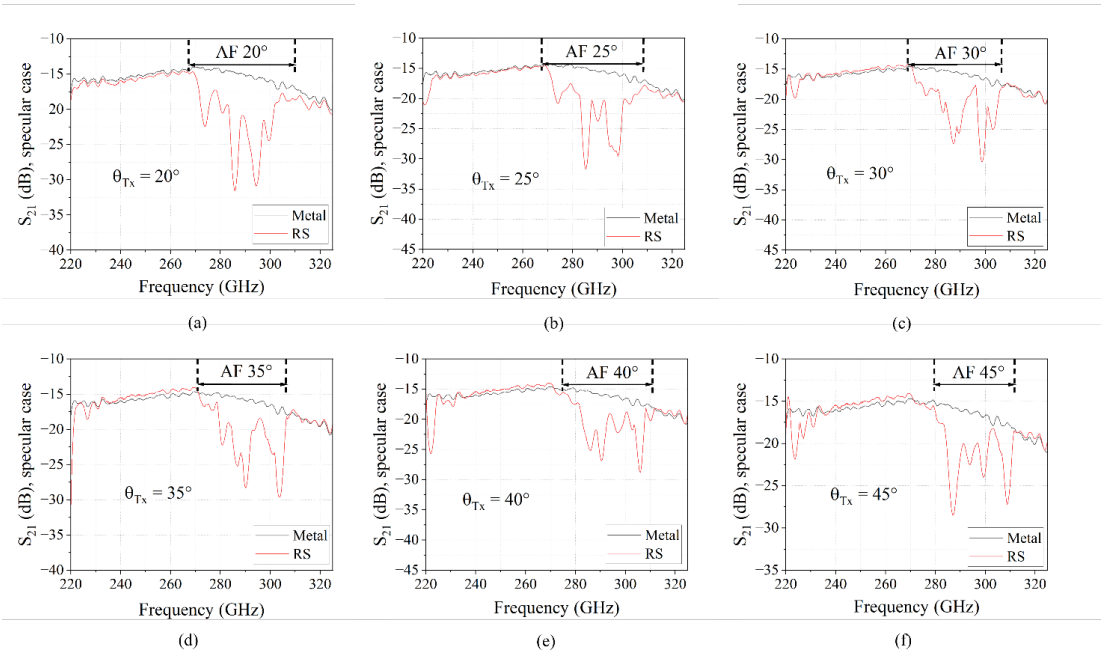

Figure 25. S_{21} amplitudes for specular reflections ($\theta_{AOA} = \theta_{AOD}$) configuration for the RS (red) and for the backside metallic plate (black) for (a) $\theta_{AOA} = 20°$, (b) 25°, (c) 30°, (d) 35°, (e) 40° and (f) 45°. The identified absorbed frequencies (AF) bandwidths in this figure show the frequency region where the RS is absorbing in the specular case.

- **Frequency band of the RS in the Nonspecular case**

The nonspecular S_{21} curves displayed in Fig. Figure 26(a)-(e) which enable to compare RS nonspecular reflections with the metal plate specular reflection. About these nonspecular reflections, two distinct patterns occur. A "quasi-specular reflection" is observed when θ_{AOA} and θ_{AOD} are close to each other (about $10°$) and a clear nonspecular reflection when angles are further from each other. Outside the RS bandwidth (270-315 GHz), a 40 dB decrease occurs for $\theta_{\mathrm{AOA}} = 20°$ between 220 and 260 GHz. In the RS bandwidth, the amplitude of the S_{21} is progressively increasing with incident angle, reaching its maximum of about -20 dB for angles $(\theta_{\mathrm{AOA}}, \theta_{\mathrm{AOD}}) = (20°, 60°)$. It confirms the RS bandwidth determined in the specular experiments.

In addition, we can clearly see the effect of moving the Rx antenna with respect to the RS. For instance, for $\theta_{\mathrm{AOA}} = 20°$, when θ_{AOA} increases we first observe a decrease of S_{21} magnitude (red and blue curves) then an increase (green and purple curves) and eventually a decrease (orange curve). Thus, in nonspecular case, we have, for each θ_{AOA}, a maximum of S_{21} for one θ_{AOD} when the angular configuration is optimal, corresponding to the optimal non-specular reflection on the RS. When the angular configuration is not optimal, a lower S_{21} is observed, which corresponds to a sub-optimal reflection case. We also observe in Figure 26(a) and (b) that for incident angles larger or equal than $15°$ and less than $30°$ we have a $40°$ shift between specular and nonspecular reflections. Besides the quasi-specular reflection which always follows the specular one, we usually have a minimum at roughly $\theta_{\mathrm{AOD}} = 40°$ and a maximum $20°$ more.

Also, when comparing with Figure 22, maximum reflection angles are close to the simulated one with Floquet theory.

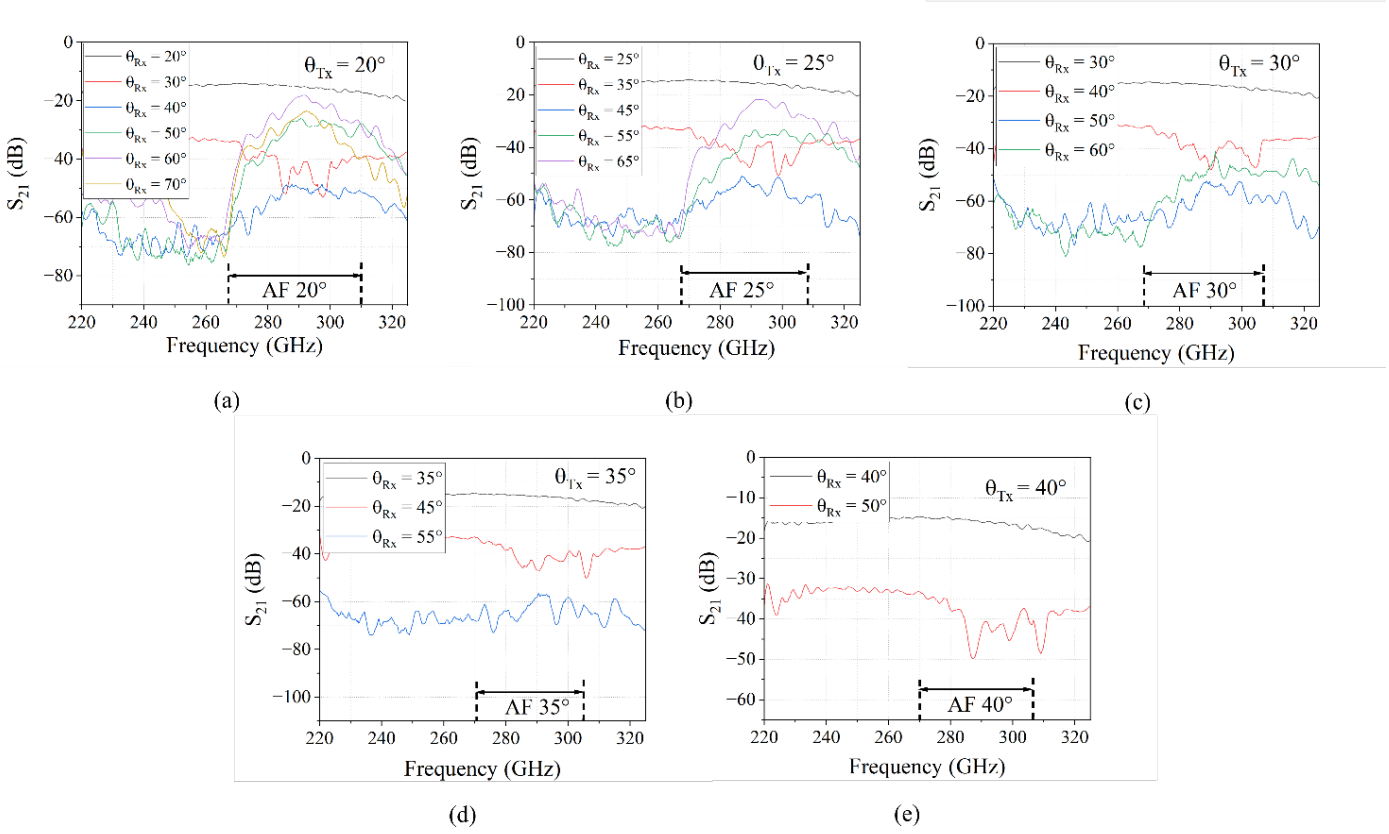

Figure 26. Comparison between S_{21} for a metallic plate specular reflection (black) and nonspecular reflections from a RS (other colors) for (a) $\theta_{AOA} = 20°$, (b) $25°$, (c) $30°$, (d) $35°$, (e) $40°$. The indicated bandwidth corresponds to the absorbed frequency (AF) range in the specular mode, see Figure 25, this frequency being then non-specularly radiated from the RS.

- **Determination of the RS losses**

As displayed in Figure 27, we zoomed on the measured S_{21} specular reflection obtained with the metallic plate (RS backside) and the highest level obtained for nonspecular reflection from the RS was reached for angles $(\theta_{\mathrm{AOA}}, \theta_{\mathrm{AOD}}) = (20°, 60°)$ between 280 and 300 GHz. The minimum loss induced by the RS is then the relative amplitude shift between the two S_{21} curves. It is found that, related to the metal plate, the lowest RS loss is about 3 dB and occurs at about 290.6 GHz. The total RS bandwidth (@3dB) is found to be about 10 GHz. However, when using the RS inside a THz data-link with a wideband signal (modulated THz data), the overall loss induced by the RS corresponds to the averaged S_{21} over the signal bandwidth, that is close to 5 GHz (see section IV). Considering the bandwidth of the modulated spectrum in Figure 27 the expected loss is about 4 dB.

In the next part, this angular configuration (minimum RS loss) serves as a basis for the use of the RS inserted in a THz wireless link.

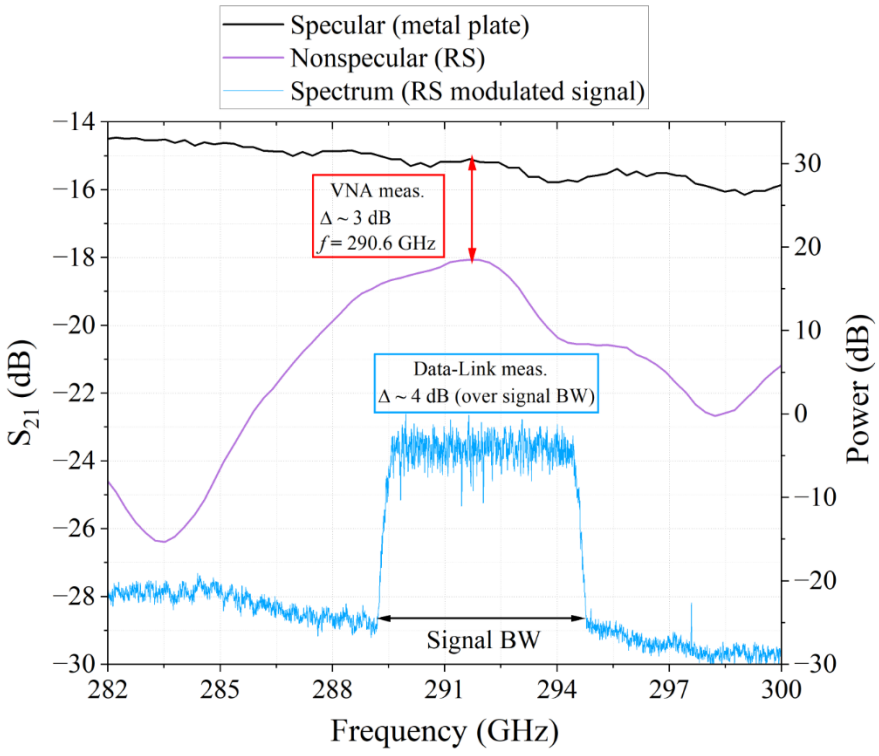

Figure 27. Zoom on the smallest measured shift between specular reflection S_{21} from the metallic plate and the nonspecular reflection one from the RS which occur for $\theta_{AOA} = 20°$ and $\theta_{AOD} = 60°$. The reference spectrum (relative power in dB) of modulated THz data used to illuminate the RS in the last section, centered at 292 GHz (see section 4).

3.3 Results for RS second prototype

- **Experimental setup description**

To characterize this new RS, we used the same setup as for the first one and depicted in the Figure 23 (a). The Figure 28 shows the new RS on the experimental setup.

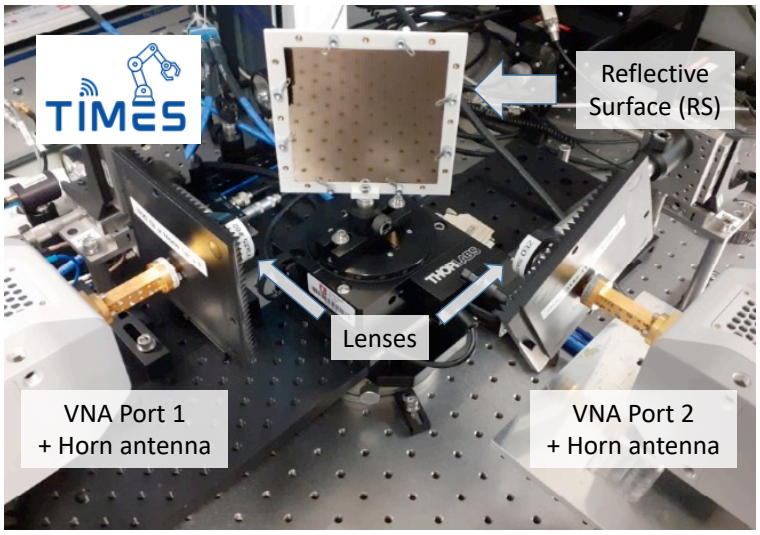

Figure 28. Photo of the VNA experimental setup for OTA characterization of the RS at 300 GHz.

In this work, we used the same experimental setup as for the one used for the RS first prototype; then, we refer the reader to the last section for everything to experimental setup.

As before, θ_{AOA} and θ_{AOD} are angle of arrival and angle of departure with respect to the normal of the RS, respectively but this time, angles are adjusted by using rotation stages with a 2° step (identical for θ_{AOA} and θ_{AOD}) and are swept from 0° to 44° for θ_{AOA} and from $-4°$ to 70° for θ_{AOD}. According to the testbed configuration, specular reflection can be measured for $\theta_{\mathrm{AOA}} = \theta_{\mathrm{AOD}}$ from 20° to 44°, which enables to assess on the angle of arrival impact on the RS frequency bandwidth, as discussed in the next section. Then, the S_{21} parameter is measured for a large number of couples $(\theta_{\mathrm{AOA}}, \theta_{\mathrm{AOD}})$ which correspond to 13 different angles of arrival and 26 different angles of departure, or 338 acquisitions for the RS and for the metal plate as reference. For each value of θ_{AOA}, we rotate the reflected VNA port to change θ_{AOD} to measure amplitude and phase of S_{21}.

- **RS bandwidth analysis by specular reflection analysis**

First, S_{21} amplitudes are compared for RS specular reflections and metal plate specular reflections (RS backside serving as reference) as well for different angles of arrival.

In Figure 29, we note, in the case of $\theta_{\mathrm{AOA}} = \theta_{\mathrm{AOD}} = 34°$, that in the specular case, the RS S_{21} only differ from metal plate between 271 GHz and 296 GHz which can be denoted as an absorption frequency (AF) range. Indeed, a clear absorbing behavior is obtained considering the S_{21} showing a large reduction of up to 34 dB. The AF range seems not to show any dependence on the AoA even though the absorption level is increasing from 15 dB ($\theta_{\mathrm{AOA}} = 20°$) to 40 dB for $\theta_{\mathrm{AOA}} = 44°$. To be more quantitative, for a given AoA, a major part of the absorbed signal in the specular configuration should reach an AoD in the nonspecular configuration (cf. Figure 30). Then, the AF range can be considered as the frequency band for which 90% of the absorbed signal flows out from the RS in a non-specular case. Fixing this criterion, the AF range is found to exceed 7 GHz for $\theta_{\mathrm{AOA}} = 34°$. Based on this preliminary analysis of the specular behavior of the RS, the next section details the RS bandwidth analysis of the non-specular reflection.

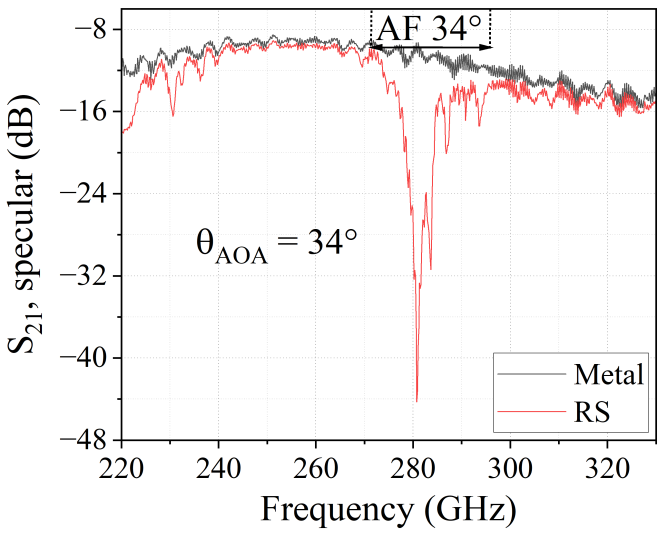

Figure 29. Example of S_{21} amplitude for specular reflection ($\theta_{AOA} = \theta_{AOD}$) configuration for the RS (red) and for the backside metallic plate (black) for $\theta_{AOA} = 34°$.

- **RS bandwidth analysis by nonspecular reflection analysis**

S_{21} curves in the nonspecular case are displayed in Figure 30 and enable to compare RS nonspecular reflections and specular reflection. Outside of the RS bandwidth (271-296 GHz), a 60 dB decreasing is occurring, for instance, for $\theta_{\mathrm{AOA}} = 34°$ between 220 and 260 GHz. Within the RS bandwidth, S_{21} amplitude is progressively increasing with angle of departure and reach is maximum of about -13 dB for the couple $(\theta_{\mathrm{AOA}}, \theta_{\mathrm{AOD}}) = (34°, 6°)$ at $f = 281.2$ GHz. This confirms the RS bandwidth determined by specular configuration experiments of the previous section.

It is also important to notice that when the angles of arrival are between 20° and 30°, the maximum of S_{21} occurs at roughly $f = 287$ GHz whereas for angles of arrival between $32°$ and $44°$, it occurs at roughly $f = 281$ GHz (cf. Figure 31).

In the nonspecular case, we have, for each θ_{AOA}, a maximum of S_{21} for a specific θ_{AOD} when the angular configuration is optimal, which is corresponding to an optimal RS nonspecular reflection. As a contrary, when the angular configuration is not optimal, a weaker S_{21} is observed, which is corresponding to a sub-optimal nonspecular reflection. In Figure 31, the maximum of S_{21} as a function of the angle of arrival is shown for $\theta_{\mathrm{AOA}} = 34°$ at $f \approx 281$ GHz. Both maxima of S_{21} are clearly seen for $\theta_{\mathrm{AOA}} = 34°$ which corresponds to the specular case and for $\theta_{\mathrm{AOD}} = 6°$ which corresponds to the best angular configuration in the nonspecular case. We thus observe a roughly a $-30°$ shift between specular case and best nonspecular case angular configurations. More generally, when the angle θ_{AOA} is between $20°$ and $30°$, this shift is close to $+40°$ whereas for θ_{AOA} between $32°$ and $44°$ the shift is more about $-30°$. Simulations were also performed and from the Floquet theory we can conclude that $+40°$ and $-30°$ shifts are related to $n = +1$ et $n = -1$ Floquet modes, respectively. In that sense, experimental results agree well with simulations. Even though, it has been observed in the simulations that for AoA $> 30°$, the structure's performance degrades because the unit cell design is intended for normal incidence (AoA $= 0°$). The presence of two modes in these measurements is in contrast with the previous RS prototype on which only the mode $n = +1$ was excited.

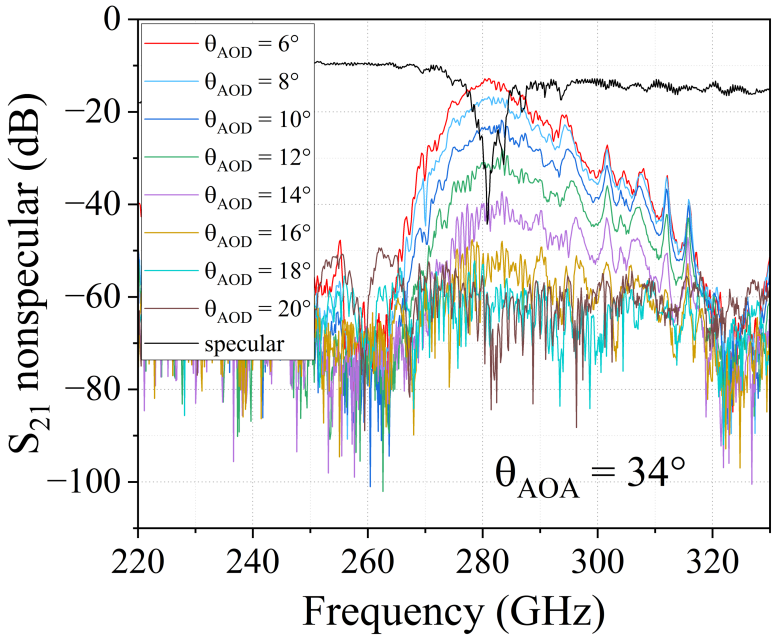

Figure 30. Comparison of S_{21} for the RS in specular reflection (black) and nonspecular reflections (other colours) for $\theta_{AOA} = 34°$.

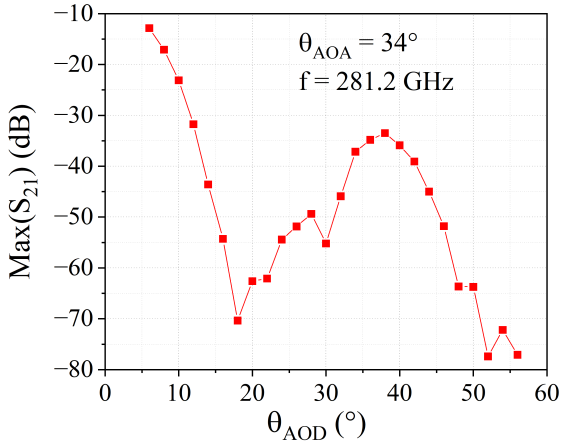

Figure 31. Evaluation of the maximum of S_{21} in terms of the angle of departure for $\theta_{AOA} = 34°$. We focused ourselves at $f = 281.2$ GHz which is the best nonspecular operation observed (maximum of S_{21}).

- **RS losses determination**

Figure 32 shows a zoom of the measured S_{21} specular reflection obtained with the metallic plate (RS backside) and the maximum of S_{21} obtained for nonspecular reflection from the RS (cf. Figure 30) between 271 and 296 GHz (AF range). It is reached for $(\theta_{\mathrm{AOA}}, \theta_{\mathrm{AOD}}) = (34°, 6°)$ The minimum loss induced by the RS is thus the relative amplitude shift between the two curves. It then shows that, related to the metallic plate, the lowest RS loss is about 1.5 dB and occurs at about 281 GHz. The obtained results can be compared with the results from the first prototype, where the RS design was different in terms of periodicity and organization of unit cells. For instance, in the specular case, the AF band and the absorption bandwidth are shorter with this new design and the S_{21} amplitude decrease is higher and depends on the angle in this case. In the nonspecular case, RS losses are less and the shift between the angle in the specular case and the best angular configuration now depends on the angle of arrival.

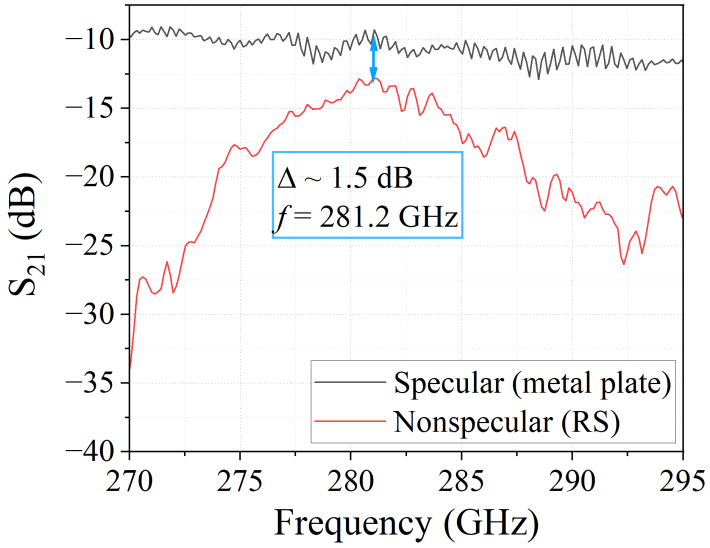

Figure 32. Zoom on the smallest measured shift between specular reflection S_{21} from the metal plate and the nonspecular reflection from the RS which occurs for $\theta_{AOA} = 34°$ and $\theta_{AOD} = 6°$.

3.4 Reconfigurable IRS

In this section the reconfigurable IRS characterization of the R-IRS is covered.

In this section, we present the results of the 280 GHz characterization of the reconfigurable RIS manufactured by Anteral, whose properties and operating principle have already been presented in the previous sections.

Since the experimental setup is the same as that used for the characteristics of the two passive RIS prototypes, we will not provide further details. We present only an image (see Figure 33) showing the reconfigurable RIS oriented horizontally to obtain the required results.

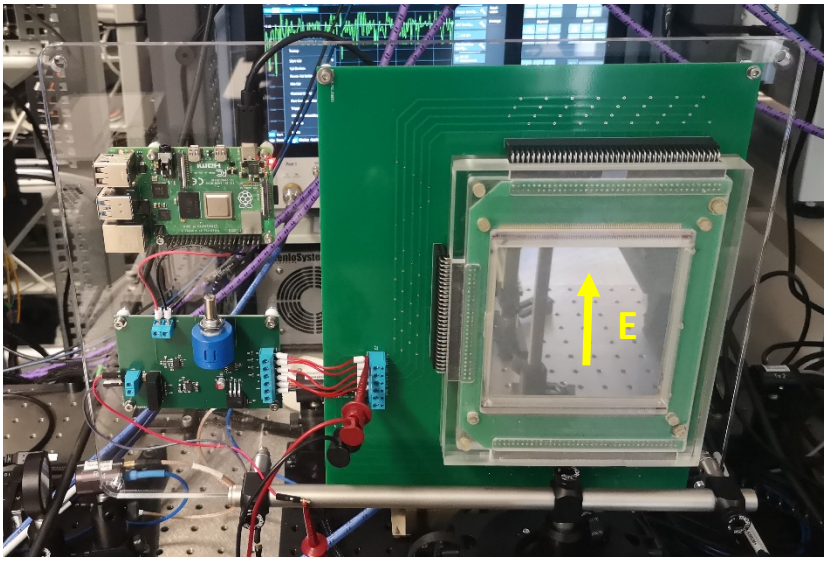

Figure 33. Photograph of the reconfigurable RIS.

In addition, we were also able to vary the peak-to-peak voltage across the electrodes which compose the RIS between 5V and 15V and observe the impact of this on the results.

Substrate response taken as reference

First, since the reconfigurable RIS has a preferred orientation as well as a preferred polarization for the incident beam, the non-compliance of these conditions allows to obtain the response of the metal substrate without worrying about the one of the liquid crystals. In the specular configuration, this therefore allowed us to obtain the reference for the measurements and this is presented in Figure 34.

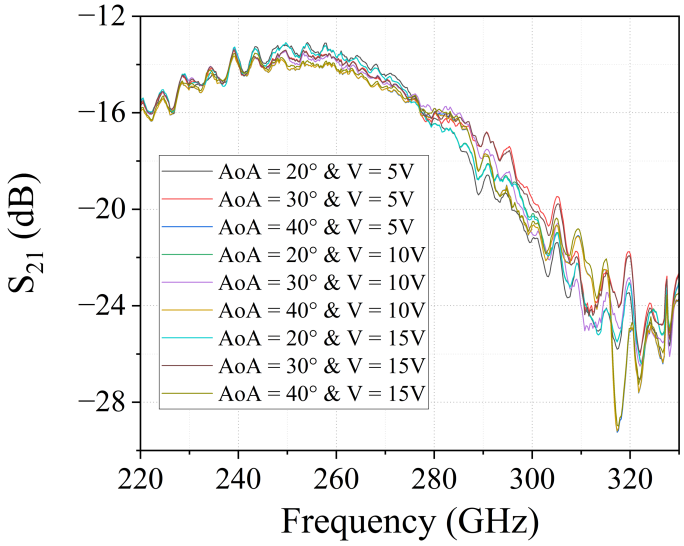

Figure 34. Amplitude of S_{21} in the specular case of the configurable RIS substrate which will be taken as a reference for different angular configurations and peak-to-peak voltages.

We thus note that the amplitude of S_{21} is approximately -16 dB at 280 GHz and does not seem to depend on the angles or the applied voltage as expected. This confirms the proposal of taking this response as a reference compared to the case where the liquid crystals actually react.

Specular configuration

Since the reconfigurable RIS must be oriented horizontally, this strongly constrains the angles for which measurements can be made, especially in the specular configuration. Thus, only two pairs of angles $(AoA = 20°, AoD = 20°)$ and $(AoA = 30°, AoD = 30°)$ could be tested for different voltages and are shown in Figure 35 (a) and Figure 35 (b).

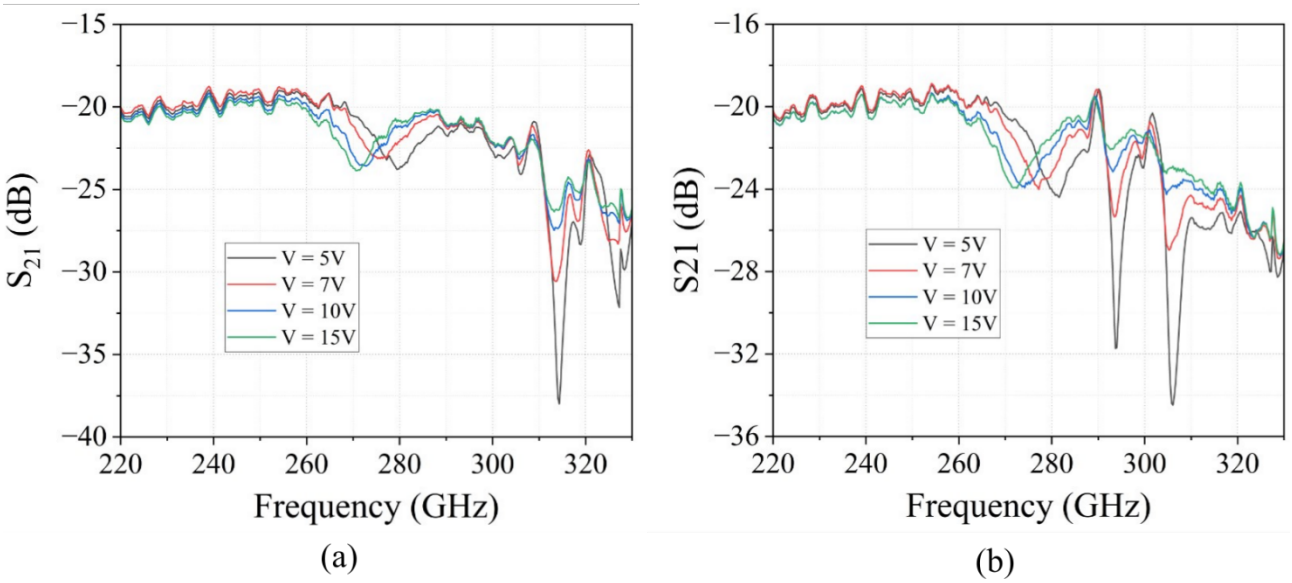

Figure 35. Amplitude of S_{21} in the specular case for (a) $AoA = AoD = 20°$ and (b) $AoA = AoD = 30°$. The different curves correspond to the different peak-to-peak voltages tested.

Several comments can be made about these curves. First, the frequency band for which there is absorption is clearly present. This absorption is on a frequency band of approximately 25 GHz (between 260 and 285 GHz) for the two pairs of angles and amplitude 4.5 dB therefore much lower than those obtained with passive RIS. Then, compared to the reference presented above (see Figure 34), the amplitude obtained in this case is 4 dB lower even in the range where the RIS response does not show any absorption. Finally, we observe, depending on the applied voltage, a frequency redshift with a greater difference observed between 5V and 7V than between 10V and 15V for example. This is a first example of confirmation of the correct operation of liquid crystals for which the voltage $V = 5V$ probably corresponds to the minimum voltage threshold while the voltage $V = 10V$ corresponds to the saturation voltage.

- **Nonspecular configuration**

After presenting the results for the specular case, we now turn to the non-specular case. Measurements were carried out for five different AoAs: 0°, 10°, 20°, 30°, and 40°, each for several AoDs and for different voltages. The AoDs are not identical for all AoAs due to experimental constraints, but they still provide a good overview.

The results are presented in Figure 36 to Figure 38 for each AoA. Each plot in each figure corresponds to a specific peak-to-peak voltage, and the substrate reference obtained previously is also displayed on the plot corresponding to an applied voltage of 5 V for comparison. We also add a fifth plot which show the maximum of S_{21} at optimal frequency against voltages for different AoDs to emphasize the difference of amplitude with voltages and AoDs.

For a maximum voltage of 15 V, the amplitude difference between the reference and the maximum reflectivity at the optimal frequency is approximately 30 dB, much higher than in the case of passive RISs, where losses did not exceed 5 dB. We then discuss the results figure by figure.

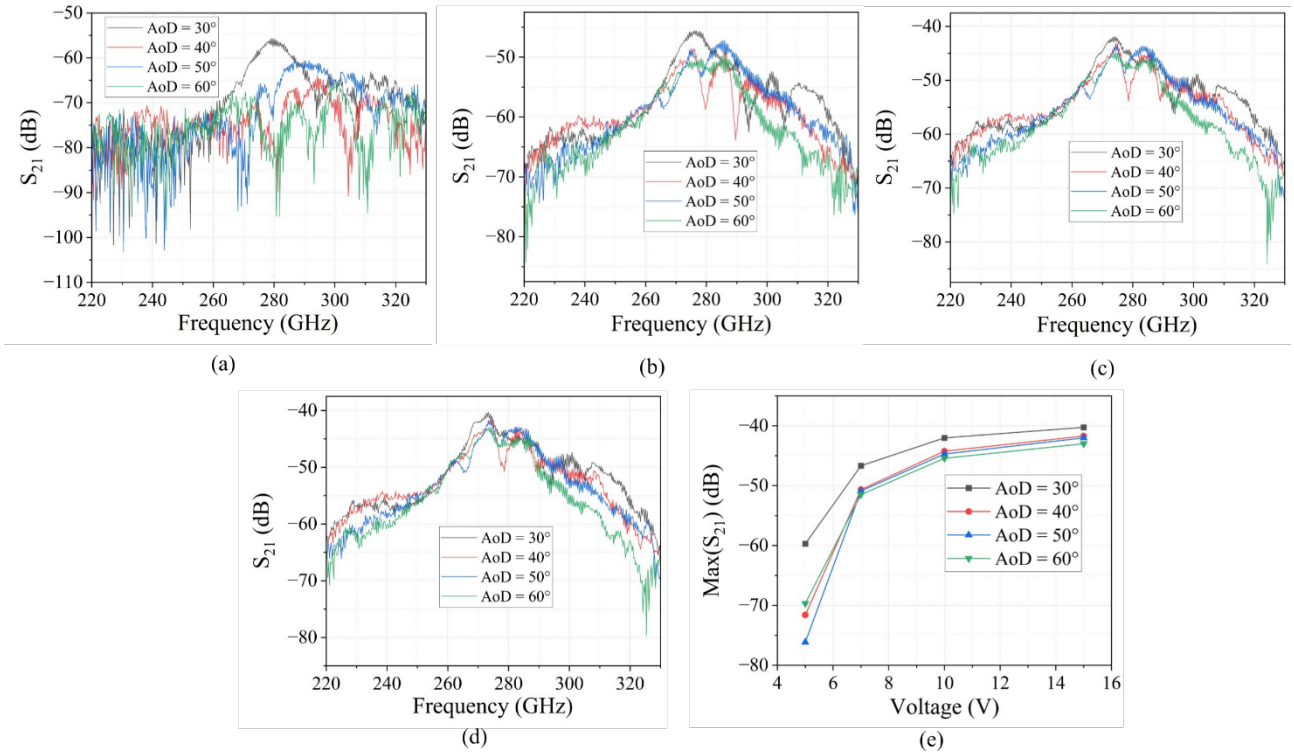

Figure 36. Amplitude of S_{21} in the non-specular case for $AoA = 0°$ for an applied voltage of (a) 5V, (b) 7V, (c) 10V and (d) 15V. (e) Maximum of S_{21} at optimal frequency $f = 273{,}35\ GHz$.

For the first Figure 36, we observe a maximum reflectivity for an $AoD = 30°$ around 280 GHz as soon as a voltage of 5 V is applied. Between 5V and 7V, the amplitude at the optimal frequency increases between -55 dB and -45 dB while between 7V and 10V, it only increases from -45 dB to -43 dB approximately. This confirms again that the saturation voltage of the liquid crystals is already reached when a voltage of 10Vpp is applied. Finally, we notice a slight frequency (blueshift, ie curve is translated to higher frequencies) when we increase the AoD at fixed AoA and voltage which is very likely to be an impact of the AoA.

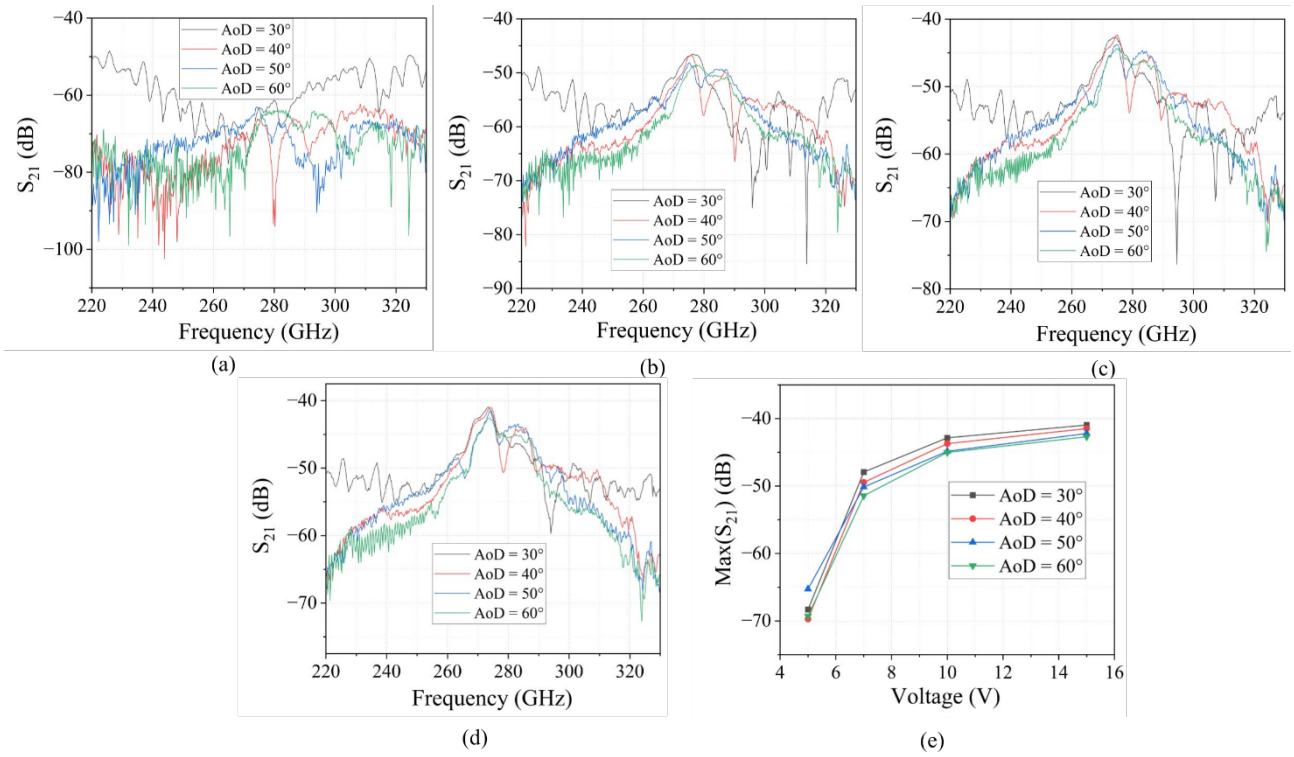

Figure 37. Amplitude of S_{21} in the non-specular case for $AoA = 10°$ for an applied voltage of (a) 5V, (b) 7V, (c) 10V and (d) 15V. (e) Maximum of S_{21} at optimal frequency $f = 273.35\ GHz$.

For the second Figure 37, the black curve (corresponding to $AoD = 30°$) seems shifted and less noisy than the other curves. In addition, and unlike the case where $AoA = 0°$, no visible reflectivity maximum is observed for a voltage of 5V. Perhaps this is an impact of the AoA on the applied voltage. Finally, the greater change in amplitude between 5V and 7V than between 7V and 10V remains present in this case and the reflectivity maximum is -41 dB at a frequency of approximately 277 GHz for an AoD of 30°.

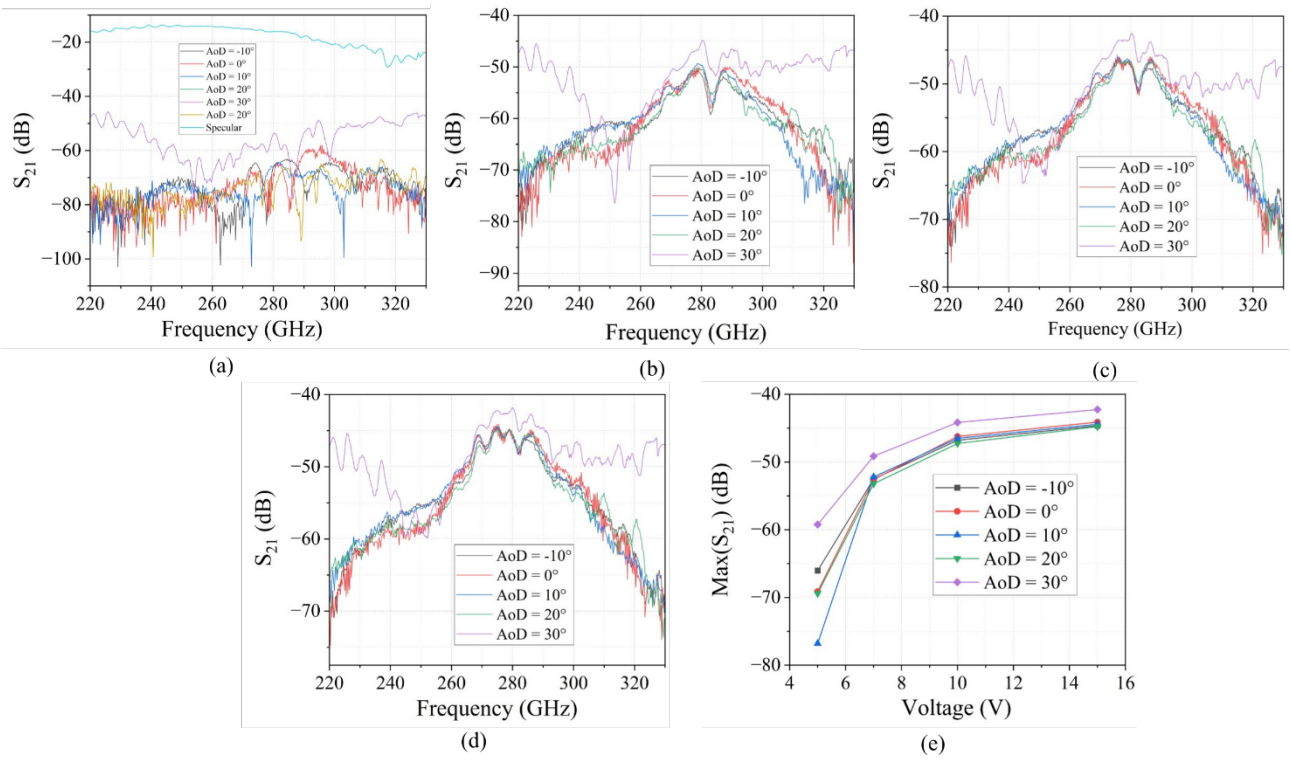

Figure 38. Amplitude of S_{21} in the non-specular case for $AoA = 40°$ for an applied voltage of (a) 5V, (b) 7V, (c) 10V and (d) 15V. (e) Maximum of S_{21} at optimal frequency $f = 275\ GHz$.

The same comments as above can be applied to the intermediate AoAs of 20° and 30°, so we present the results directly for $AoA = 40°$ in Figure 38. In this case, the maximum reflectivity remains around -45 dB at a frequency of around 280 GHz for an AoD of 0° if we do not take into account the purple curve which again presents a different behavior from the other curves and seems to be closer to the response in the specular case.

▪ Conclusion of the R-IRS measurements

In the light of the R-IRS measurements, we can conclude that:

- The absorption band of the R-IRS is matching to the design, as per the simulation curves shown. The phase profile of the R-IRS is coherent with the localized best operation bandwidth found around 275-280 GHz.
- The effect of the liquid crystal is clearly obtained, confirming the permittivity change, and induced frequency shift on the absorption bandwidth.
- The non-specular operation of the R-IRS is obtained, with a clear effect of the level of the reflectivity observed. However, the reflectivity value obtained is lower than expected, and a loss (specular/non specular contrast) of about 20-25 dB is obtained, depending of the applied voltage. A very small effect on the non specular beam level is obtained: the main direction is not strongly affected by the applied voltage.

We can also mention that the R-IRS can be used as a switch, as the variation of the S21 is strongly depending on the applied (figure 27 for AoA = 0°, normal incidence).

4 Terahertz Data-Links Including IRS

4.1 Testbed description

To enable the test of the THz data link, the 2 VNA heads of Figure 23(b) are replaced by a modulated signal source used instead of VNA port 1 (P1 in Figure 23(b)), and the receiver circuits are placed in place of the VNA port 2 (P2). A schematic diagram of the transmit and receive units is given in Figure 39. Here, the photomixing method is used to generate THz modulated signals, leveraging the techniques widely used in fiber-optic communications. The transmitter is using two continuous wave (CW) lasers, one is modulated, and the other one is CW. The optically modulated one is obtained using I and Q baseband signals to drive an optical IQ Mach-Zehnder modulator (MZM). This results in an optical quadrature phase shift keying (QPSK) or quadrature amplitude modulation with 16 states (QAM-16). The baud-rate used is fixed and set to 5 GBaud considering the RS available bandwidth. The fiber output of the MZM is combined with the CW laser which acts as a local oscillator. The lasers are free-running, with an intrinsic instantaneous linewidth of 10 kHz. This optical signal is amplified thanks to an erbium doped fiber amplifier (EDFA), to further feed a waveguide output UTC-PD, connected to the WR3.4 horn antenna. Using a 292 GHz detuning of the lasers enables to generate a 292 GHz signal at photomixer output.

It should be noted that the 292 GHz frequency was chosen to get optimum performances considering the testing system (transmit/receive system in back-to-back mode) [5].

The signal is then propagated in the over-the-air (OTA) case, using the same THz configuration than the one used for RS measurements (cf. Figure 23(b)). At the receiver side, the 292 GHz is down-converted using an electrically pumped subharmonic mixer (SHM) (WR2.8 model from VDI) allowing the modulated THz signal to be down-converted into an intermediate frequency (IF) $<$40 GHz. The roll-off effect of the SHM (frequency dependence of the IF path in the SHM and IF amplifier gain) is corrected during equalization applied during the signal analysis. The SHM requires a LO tone around 150 GHz which is provided by a signal generator (SMA100B from Rohde & Schwarz) with a subsequent $\times$12 multiplier. The IF signal is then first amplified (SHF 810 model from SHF) and captured by a 70 GHz real-time oscilloscope. (UXR Keysight). This enables a real-time analysis of the usual performance metrics such as the error vector magnitude (EVM).

The signal processing applied in the experiments is the following: first, typically short (below 1 µs) scale time frames are sampled in order to limit the effect of the lasers phase noise on the IQ map. The local oscillator is adjusted to get a center IF frequency at a value which is far from 0 Hz (typically 10.5 GHz) to enable a direct demodulation of the IQ signal using the commercial “digital demodulation” tool embedded in the Keysight Pathwave Vector Signal Analysis (89600 VSA software), to compute the signals EVM (Error Vector Magnitude).

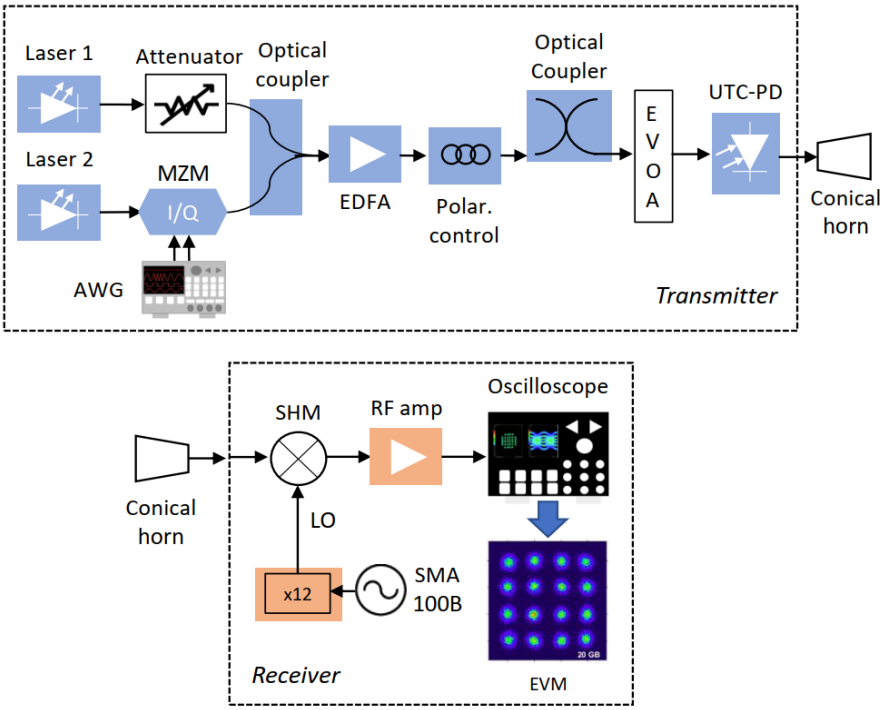

Figure 39. Experimental setup of the insertion of the RS within the THz data-link. Transmitter and receiver placed in place of VNA ports 1 and 2 of Figure 23 (b), respectively.

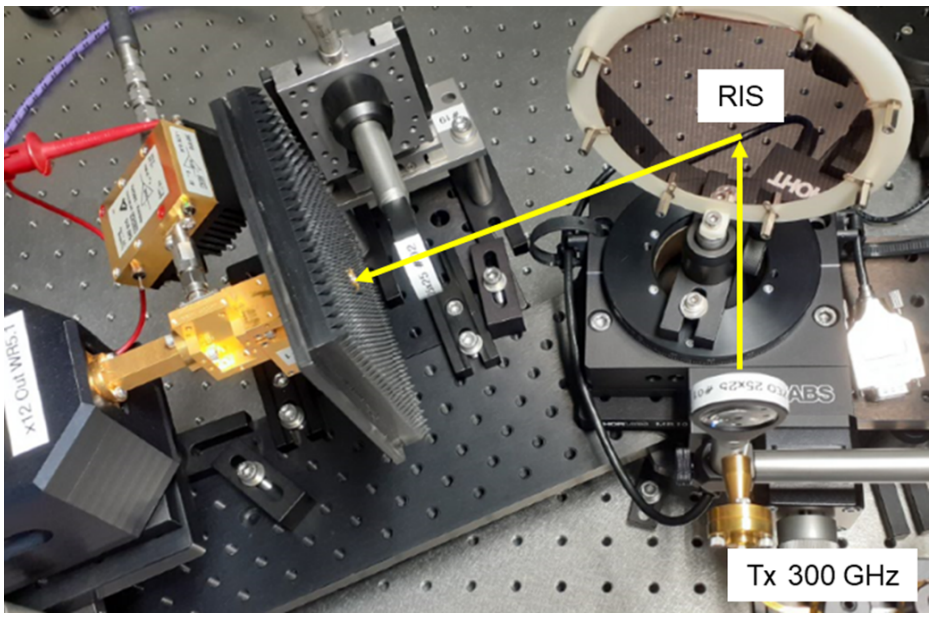

Figure 40. Experimental setup of the THz link enabled by the RS.

4.2 Fixed IRS

First, the system is optimized in terms of EVM in back-to-back (B2B), where transmit and receive circuits are directly waveguide connected to each other, using a 292 GHz carrier frequency. To be able to analyze the penalty induced by the RS in the OTA configuration, we compare the EVM performance of the link using the specular reflection on the metal plate and the case of nonspecular reflection on the RS. In both cases, the EVM is measured as function of the relative received power (power difference between B2B and OTA transmission), enabling to assess the power penalty (power shift to obtain the same EVM in each case) induced by the RS in the best angular configuration determined in the last section.

Figure 41(a) and (b) shows the results for a QPSK and QAM-16 at 5 GBaud, for both specular cases (backside of the RS serving as metal plate) and nonspecular reflection on RS. We can clearly see that the behavior is very similar, shifted in the x-axis. The power penalty is found to be about 6 dB. Comparing with OTA measurements with VNA, as discussed before we could expect at least a 4 dB penalty. However, a higher penalty is obtained, but 4 dB estimation did not consider some beam modifications or other specific effects due to the RS. In any case, this validates the insertion of the RS within the THz link, with a 6 dB penalty for NLoS THz link.

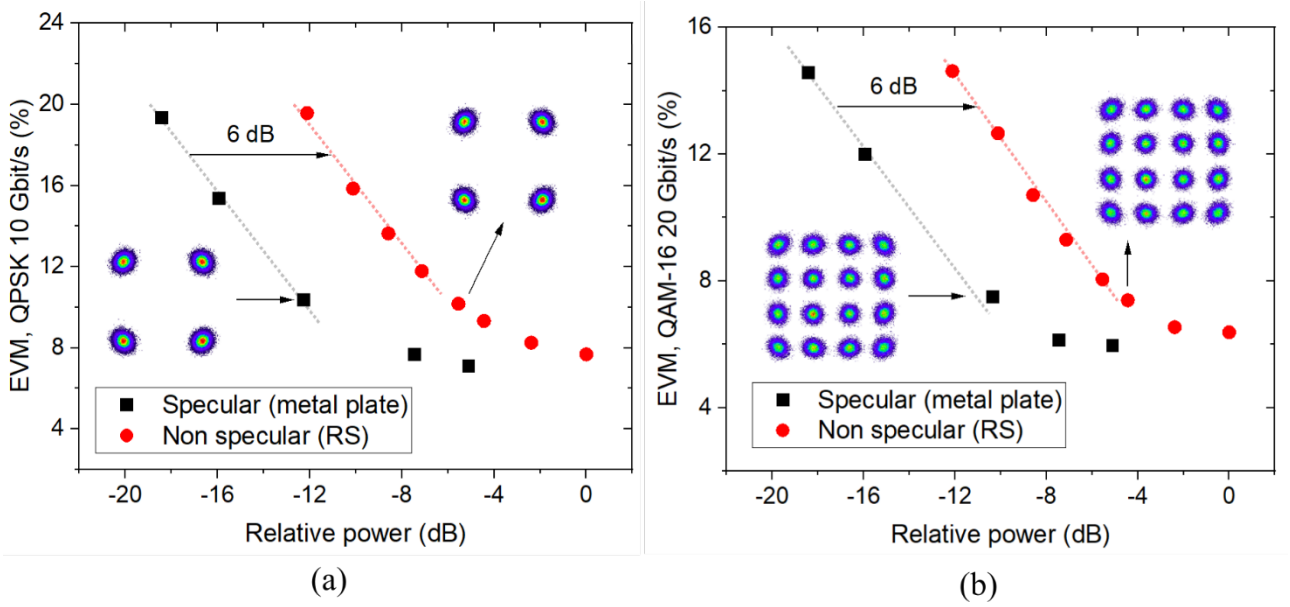

Figure 41. (a) EVMs for RS and metallic plate for a QSPK modulation with a 10 Gbits/s data rate and (b) a QAM-16 modulation with a 20 Gbits/s data rate with carrier frequency of 292 GHz, together with the representative IQ constellation diagrams. Dotted lines are linear trend used to determine the power penalty, found to be about 6 dB in both cases.

5 Conclusions

The RIS designs and characterizations were presented on this deliverable as part of the TIMES activities related to the potential use of IRS at THz frequencies. The designs and characterization methods have been described, and applied for IRS fabrication and characterization.

For static IRS, ie RS devices, the behavior of the OTA device is found to be in line with simulations. Related to this devices, the bandwidth of the specular absorption has shown a very good coherence with the non-specular response. Furthermore, the proposed method enabled to assess the RS losses to be only a few dB, compared to a pure reflector. Among the two proposed designs, the second one that showed the best performances was chosen for the proof of concept 1 (PoC1) using FDD modems in the static configuration depicted in the WP2.

The operation of the R-IRS was validated, however higher losses are obtained at this moment. Such losses level is to be checked with the available link budgets in the PoCs. Beyond the loss level, the variation of angular of departure (AoD) is not controllable with the R-IRS control voltage, but the non-specular reflectivity level is tunable, even if lossy. The R-IRS could then be used as a switch and potential laboratory validation could confirm this if enough output power is available from amplifiers.

6 References

[1] Hou-Tong Chen, Hao Yang, Ranjan Singh, John F. O'Hara, Abul K. Azad, Stuart A. Trugman, Q. X. Jia and Antoinette J. Taylor, "Tuning the Resonance in High-Temperature Superconducting Terahertz Metamaterials", Phys. Rev. Lett. 105, 247402 – DOI: https://doi.org/10.1103/PhysRevLett.105.247402.

[2] T. Niu, J. Zhang, L. Cheng, P. Cao, R. Cui and Z. Mei, "Reconfigurable Terahertz Reflectarray Based on Graphene Radiating Patches," 2020 14th European Conference on Antennas and Propagation (EuCAP), Copenhagen, Denmark, 2020, pp. 1-4, doi: 10.23919/EuCAP48036.2020.9135393.

[3] Dibakar Roy Chowdhury, Ranjan Singh, John F. O'Hara, Hou-Tong Chen, Antoinette J. Taylor, Abul K. Azad; Dynamically reconfigurable terahertz metamaterial through photo-doped semiconductor. Appl. Phys. Lett. 5 December 2011; 99 (23): 231101. https://doi.org/10.1063/1.3667197.

[4] M. A. Pulido-Gaytán, J. A. Reynoso-Hernández, J. R. Loo-Yau, A. Zárate-de Landa and M. d. C. Maya-Sánchez, "Generalized Theory of the Thru-Reflect-Match Calibration Technique," in IEEE Transactions on Microwave Theory and Techniques, vol. 63, no. 5, pp. 1693-1699, May 2015, doi: 10.1109/TMTT.2015.2417860.

[5] F. Dutin, U. B. Gartzia, V. Torres, P. Szriftgiser, J. Teniente and G. Ducournau, "Non-Line-of-Sight 300 GHz Band Wireless Link Enabled by a Frequency Dependent Reflective Surface," in IEEE Transactions on Terahertz Science and Technology, vol. 15, no. 3, pp. 400-411, May 2025, doi: 10.1109/TTHZ.2025.3539501.